NATIONAL OPTICAL ASTRONOMY OBSERVATORIES

Preprint Series

NOAO Preprint No. 834

WFPC2 OBSERVATIONS OF THE URSA MINOR DWARF SPHEROIDAL GALAXY

KENNETH J. MIGHELL
CHRISTOPHER J. BURKE

To Appear In: The Astrophysical Journal

March 1999

Operated for the National Science Foundation by the Association of Universities for Research in Astronomy, Inc.

To appear in the Astronomical Journal (accepted 1999 March 1)

WFPC2 OBSERVATIONS OF THE URSA MINOR DWARF SPHEROIDAL GALAXY[1]

KENNETH J. MIGHELL[2] AND CHRISTOPHER J. BURKE[3,4]
Kitt Peak National Observatory, National Optical Astronomy Observatories[5],
P. O. Box 26732, Tucson, AZ 85726
mighell@noao.edu, christopher.burke@yale.edu

[1]Based on observations made with the NASA/ESA *Hubble Space Telescope*, obtained from the data archive at the Space Telescope Science Institute, which is operated by the Association of Universities for Research in Astronomy, Inc. under NASA contract NAS5-26555.

[2]Guest User, Canadian Astronomy Data Centre, which is operated by the Dominion Astrophysical Observatory for the National Research Council of Canada's Herzberg Institute of Astrophysics.

[3]Based on research conducted at NOAO as part of the Research Experiences for Undergraduates program.

[4]*Current address:* Department of Astronomy, Yale University, P. O. Box 208101, New Haven, CT 06520-8101

[5]NOAO is operated by the Association of Universities for Research in Astronomy, Inc., under cooperative agreement with the National Science Foundation.

ABSTRACT

We present our analysis of archival *Hubble Space Telescope* Wide Field Planetary Camera 2 (WFPC2) observations in F555W (∼V) and F814W (∼I) of the central region of the Ursa Minor dwarf spheroidal galaxy. The V versus $V-I$ color-magnitude diagram features a sparsely populated blue horizontal branch, a steep thin red giant branch, and a narrow subgiant branch. The main sequence reaches ∼2 magnitudes below the main-sequence turnoff ($V_{\rm TO}^{\rm UMi} \approx 23.27 \pm 0.11$ mag) of the median stellar population. We compare the fiducial sequence of Ursa Minor with the fiducial sequence of the Galactic globular cluster M92 (NGC 6341). The excellent match between Ursa Minor and M92 confirms that the median stellar population of the UMi dSph galaxy is metal poor ([Fe/H]$_{\rm UMi} \approx$ [Fe/H]$_{\rm M92} \approx -2.2$ dex) and ancient ($age_{\rm UMi} \approx age_{\rm M92} \approx 14$ Gyr). The $B-V$ reddening and the absorption in V are estimated to be $E(B-V) = 0.03 \pm 0.01$ mag and $A_V^{\rm UMi} = 0.09 \pm 0.03$ mag. A new estimate of the distance modulus of Ursa Minor, $(m-M)_0^{\rm UMi} = 19.18 \pm 0.12$ mag, has been derived based on fiducial-sequence fitting with M92 [$\Delta V_{\rm UMi-M92} = 4.60 \pm 0.03$ mag and $\Delta(V-I)_{\rm UMi-M92} = 0.010 \pm 0.005$ mag] and the adoption of the apparent V distance modulus for M92 of $(m-M)_V^{\rm M92} = 14.67 \pm 0.08$ mag (Pont et al. 1998, A&A, 329, 87). The Ursa Minor dwarf spheroidal galaxy is then at a distance of 69 ± 4 kpc from the Sun. These *HST* observations indicate that Ursa Minor has had a very simple star formation history consisting mainly of a single major burst of star formation about 14 Gyr ago which lasted $\lesssim$2 Gyr. While we may have missed minor younger stellar populations due to the small field-of-view of the WFPC2 instrument, these observations clearly show that most of the stars in the central region Ursa Minor dwarf spheroidal galaxy are ancient. If the ancient Galactic globular clusters, like M92, formed concurrently with the early formation of the Milky Way galaxy itself, then the Ursa Minor dwarf spheroidal is probably as old as the Milky Way.

Subject headings: galaxies: abundances — galaxies: evolution – galaxies: individual (Ursa Minor) – Local Group

1. INTRODUCTION

The Ursa Minor (UMi) dwarf spheroidal (dSph) galaxy was independently discovered by Wilson (1955) and Hubble. Ursa Minor is the second closest satellite galaxy of the Milky Way at a distance of 69±4 kpc (~220,000 light years) from the Sun. Color-magnitude diagrams of the brightest stars of this faint ($M_V \approx -8.9$ mag: Kleyna et al. 1998) small ($r_{\rm tidal} = 628 \pm 74$ pc: Irwin & Hatzidimitriou 1995) galaxy feature a strong blue horizontal branch (e.g., van Agt 1967; Cudworth, Olszewski, & Schommer 1986; Kleyna, et al. 1998) — a unique horizontal branch morphology amongst the nine Galactic dSph satellite galaxies. The deep BV CCD observations of Olszewski & Aaronson (1985) indicate that Ursa Minor has an age and abundance very similar to that of the ancient metal-poor Galactic globular cluster M92 (NGC 6341). Ursa Minor may be the only dwarf galaxy in the Local Group which is composed exclusively of stars older than 10 Gyr (Mateo 1998).

In this work we investigate the star formation history of the Ursa Minor spheroidal galaxy using archival *Hubble Space Telescope* WFPC2 data. Section 2 is a discussion of the observations and photometric reductions. We present and compare our results with previous work in Sec. 3. The paper is summarized in Sec. 4. Appendix A describes a new robust algorithm for the computation of of fiducial sequences from high-quality stellar photometry.

2. OBSERVATIONS AND PHOTOMETRY

The Ursa Minor dwarf spheroidal galaxy was observed with the *Hubble Space Telescope* (*HST*) Wide Field Planetary Camera 2 (WFPC2) on 1995 July 4 through the F555W (~V) and F814W (~I) filters. The WFPC2 WFALL aperture (Biretta et al. 1996) was centered on the target position given in Table 1 and shown in Figure 1. Two low-gain observations were obtained in each filter. These observations were secured as part of the *HST* Cycle 5 program GTO/WFC 6282 (PI: Westphal) and were placed in the public data archive at the Space Telescope Science Institute on 1996 July 5. The datasets were recalibrated at the Canadian Astronomy Data Centre and retrieved electronically by us using a guest account which was kindly established for KJM.

These WFPC2 observations contain several types of image defects. Figure 2 shows a negative mosaic image of the U2PB0103T dataset. Besides exhibiting normal cosmic ray damage, this 1100-s F555W exposure also shows (1) a satellite trail on the WF4 CCD, (2) an elevated background near the inner corner of the PC1 CCD, and (3) shadows are seen on all four CCDs. The elevated background near the inner-corner of the PC1 CCD is probably due to stray light patterns from a bright star just outside of the PC1 field-of-view (cf. Fig. 7.1.a of Biretta, Ritchie, & Rudloff 1995). The shadows seen on all four CCDs are indicative of a serious problem with these observations because the shadows are generally seen against an elevated background throughout the entire WFPC2 field-of-view. This phenomenon is due to light from the bright sun-lit Earth reflecting off the optical telescope assembly (OTA) baffles and the secondary mirror supports

("spider") and into the WFPC2 instrument. Elevated backgrounds occur when the angle between the Earth and the OTA axis is <25 degrees (cf. Fig. 11.2.a of Biretta et al. 1995). The background "sky" brightened significantly during the course of these observations (see Figure 3) indicating that the *Hubble Space Telescope* experienced earthrise during these WFPC2 observations of the Ursa Minor dwarf spheroidal galaxy.

The experimental design of these WFPC2 observations was nearly identical to that of the Carina dwarf spheroidal program GTO/WFC 5637 (PI: Westphal) which was analyzed by Mighell (1997). We therefore planned to follow Mighell's Carina photometric reduction procedures in this investigation of the Ursa Minor dwarf spheroidal. Unfortunately, the standard cosmic-ray removal procedure failed spectacularly due to earthrise causing the background sky level to change rapidly. We had to improvise more complicated analysis techniques than ones used by Mighell in his Carina study in order to obtain stellar photometry of comparable quality.

We found stellar candidates on cosmic-ray cleaned images which were suitable for the detection of point sources but unsuitable for further photometric analysis. The cosmic rays were removed by using the CRREJ task of the IRAF STSDAS.HST_CALIB.WFPC package with the sky subtraction parameter set to SKY=MODE instead of the default value of SKY=NONE — this unusual option was required because the sky levels of the observations did not scale with exposure time. We used CRREJ to make a clean F555W observation of 2100 s from the U2PB0102T and U2PB0103T datasets and a clean F814W observation of 2300 s from the U2PB0105T and U2PB0106T datasets. Figure 4 shows that this procedure repaired most of the cosmic-ray damage seen in Figure 2. This procedure is clearly not perfect since traces of the satellite trial are still visible. The SKY=MODE option produces cosmic-ray cleaned images with modal pixel values near zero. Many background pixels will thus have negative values which implies negative background-flux values. Such physically unrealistic background data values are quite rightly rejected by many standard CCD stellar photometry packages.

Unsharp mask images of the clean F555W and F814W observations were made using the LPD (low-pass difference) digital filter which was designed by Mighell to optimize the detection of faint stars in *HST* WF/PC and WFPC2 images (Appendix A of Mighell & Rich 1995, and references therein). The F555W unsharp mask image (see Figure 5) and the F814W unsharp mask image were then added together to create a master unsharp mask image of each WF CCD. A simple peak detector algorithm was then used on the master unsharp images to create a list of point source candidates with coordinates $60 \leq x \leq 790$ and $60 \leq y \leq 790$ on each WF CCD. This allowed the use of almost the entire field-of-view of each WF camera while avoiding edge-effects in the outer regions. We only present the analysis of data obtained from the WF cameras in this paper.

The data were analyzed with the CCDCAP[6] digital circular aperture photometry code developed by Mighell to analyze *HST* WFPC2 observations (Mighell et al. 1997, and references therein). A fixed aperture with a radius of 2.5 pixels was used for all stars on the WF CCDs. The local background level was determined from a robust estimate of the mean intensity value of all pixels between 2.5 and 6.0 pixels from the center of the circular stellar aperture. Point source candidates were rejected if either (1) the measured signal-to-noise ratio of either instrumental magnitude was SNR<10; or (2) the center of the aperture [which was allowed to move in order to maximize the SNR] changed by more than 1.8 pixels from its detected position on the master unsharp mask. The Charge Transfer Effect was removed from the instrumental magnitudes by using a 4% uniform wedge along the Y-axis of each CCD as described in Holtzman et al. (1995b). We used the standard WFPC2 magnitude system (Holtzman et al. 1995b) which is defined using $1''$ diameter apertures. We measured the stars with a smaller aperture ($0.5''$ diameter) in order to optimize the measured stellar signal-to-noise ratios; usage of $1''$ diameter apertures resulted in significantly poorer photometry for the faint stars. The instrumental magnitudes, v_r and i_r, were transformed to Johnson V and Cousins I magnitudes using the following equations $V = v_r + \Delta_r + \delta_r + [-0.052 \pm 0.007](V-I) + [0.027 \pm 0.002](V-I)^2 + [21.725 \pm 0.005]$ and $I = i_r + \Delta_r + \delta_r + [-0.062 \pm 0.009](V-I) + [0.025 \pm 0.002](V-I)^2 + [20.839 \pm 0.006]$ where an instrumental magnitude of zero is defined as one DN s^{-1} at the high gain state ($\sim$14 e^- DN^{-1}). The constants come from Table 7 of Holtzman et al. (1995b). The values for average aperture corrections[7] , $\langle \Delta_r \rangle$, for each filter/CCD combination are listed in Table 2. The zero-order ("breathing") aperture corrections[8] for these observations (δ_r : see Table 3) were computed using

---

[6]IRAF implementations of CCDCAP are now available over the Wide World Web at the following site: http://www.noao.edu/staff/mighell/ccdcap/

[7]Observed WFPC2 point spread functions (PSFs) vary significantly with wavelength, field position, and time (Holtzman et al. 1995a). There were not enough bright isolated stars in these WFPC2 observations to adequately measure the variation of the point spread function across each WF CCD using the observations themselves. We measured artificial point spread functions synthesized by the TINY TIM VERSION 4.4 software package (Krist 1993, Krist & Hook 1997) to determine the aperture corrections, Δ_r, required to convert instrumental magnitudes measured with an aperture of radius 2.5 pixels to a standard aperture of radius 5.0 pixels ($1''$ diameter). A catalog of 289 synthetic point spread functions of a G-type star was created with a 17×17 square grid for each filter (F555W and F814W) and CCD (WF2, WF3, and WF4). The spatial resolution of one synthetic PSF every 50 pixels in x and y allowed for the determination of aperture corrections for any star in the entire WFPC2 field-of-view to have a spatial resolution of $\lesssim$35 pixels.

[8]Spacecraft jitter during exposures and small focus changes caused by the *HST* expanding and contracting ("breathing") once every orbit are another two important causes of variability in observed WFPC2 point spread functions. These temporal variations of WFPC2 PSFs can cause small, but significant, systematic offsets in the photometric zeropoints when small apertures are used. Fortunately, these systematic offsets can be easily calibrated away by simply measuring bright isolated stars on each CCD twice: once with the small aperture and again with a larger aperture. The robust mean magnitude difference between the large and small apertures is then the zero-order aperture correction, δ_r, for the small aperture which, by definition, can be positive or negative. Zero-order aperture corrections are generally small for long exposures, however, they can be quite large for short exposures that were obtained while the WFPC2 was slightly out of focus (by a few microns) due to the expansion/contraction of the *HST*

a large aperture with a radius of 3.5 pixels and a background annulus of $3.5 \leq r_{\rm sky} \leq 7.0$ pixels.

Two (V, I) datasets pairs, (U2PB0102T, U2PB0105T) and (U2PB0103T, U2PB0106T), were reduced independently using CCDCAP and the resulting instrumental magnitudes were transformed to Johnson V and Cousins I magnitudes. We determined which objects probably had acceptable photometry from these independent measurements. The V measurements of a star, V_1 [$\Leftarrow$ (U2PB0102T, U2PB0105T)] and V_2 [$\Leftarrow$ (U2PB0103T, U2PB0106T)], with photometric errors, σ_{V_1} and σ_{V_2}, were determined to be acceptable if the following condition was true: $|V_1 - V_2| \leq \max\left(\left[3\sqrt{2}\min(\sigma_{V_1}, \sigma_{V_2})\right], 0.06\right)$. If the condition was satisfied, we then adopted the quantity, $\max(V_1, V_2) - 2.5\log\left[(1 + \{10^{0.4}\}^{|V_1 - V_2|})/2\right]$, as the V magnitude of the star and adopted the quantity, $\sqrt{(\sigma_{V_1}^2 + \sigma_{V_2}^2)/2}$, as a conservative estimate of its V photometric error, σ_V. We assumed that cosmic rays would be the primary cause of poor photometry and therefore adopted the photometry of the faintest measurement of the star whenever the acceptability condition failed. The adopted I magnitude and I photometric error, σ_I, was determined from both I measurements, I_1 [$\Leftarrow$ (U2PB0102T, U2PB0105T)] and I_2 [$\Leftarrow$ (U2PB0103T, U2PB0106T)], in an analogous manner. Figure 6 shows the outlier measurements we have identified in this manner. Figure 7 gives our preliminary V versus $V - I$ color-magnitude diagram CMD of the observed stellar field in Ursa Minor dwarf spheroidal galaxy.

We present our WFPC2 stellar photometry of 696 stars in the central region of the Ursa Minor dwarf spheroidal galaxy in Table 4. The first column gives the identification (ID) of the star. The second and third columns give the V magnitude and its rms ($1\,\sigma$) photometric error σ_V. Likewise, the fourth and fifth columns give the $V-I$ color and its rms ($1\,\sigma$) photometric error $\sigma_{(V-I)}$. The sixth column gives the quality flag value of the star. We only present photometry of stars with signal-to-noise ratios SNR ≥ 10 in both the F555W and F814W filters.

3. DISCUSSION

3.1. Color-Magnitude Diagram

The V versus $V-I$ color-magnitude diagram of the observed stellar field in Ursa Minor is shown in Figure 8. This CMD features a sparsely populated blue horizontal branch, a steep thin red giant branch, and a narrow subgiant branch. The main sequence reaches ~2 magnitudes below the turnoff of the main stellar population of the Ursa Minor galaxy.

Figure 8 shows a small amount of foreground contamination by foreground stars in our Galaxy. Ratnatunga & Bahcall (1985) used the Bahcall and Soneira Galaxy model (Bahcall & Soneira 1980, 1980; Bahcall et al. 1980) to predict that 2.3 foreground stars brighter than $V = 25$

---

during its normal breathing cycle.

mag would be found in one square arcmin in the direction of Ursa Minor. Our observation surveys 4.44 arcmin^2 of Ursa Minor and we would therefore expect, from the prediction of Ratnatunga and Bahcall, to find ~10 foreground stars brighter than $V = 25$ mag in our color-magnitude diagrams. A direct check with observations is provided by Figure 2 of Kleyna et al. (1998) which indicates that while foreground contamination towards Ursa Minor is small it can not be ignored. The 4 bright blue stars near $V \approx 20$ mag with colors $(V-I) < 0.3$ mag will be shown below to be probable Ursa Minor horizontal branch stars. There are a few fainter blue stars seen in Fig. 8 which are within $\lesssim$2 magnitudes of the main-sequence turnoff of the main Ursa Minor stellar population. Determining whether these "blue stragglers" are actually members of the Ursa Minor galaxy or are simply Galactic foreground stars is beyond the scope of this paper.

3.2. Fiducial Sequence

The robust median $V-I$ color as a function of V magnitude of the Ursa Minor main sequence, subgiant branch, and base of the red giant branch ($21.5 \leq V \leq 25.0$ mag) is listed in Table 5 and shown in Figure 9. The robust median $V-I$ color of a given $\Delta V = 0.2$ mag data subsample was determined after $\gtrsim 2.4\sigma$ outliers were iteratively rejected in 5 iterations of a robust fiducial sequence algorithm (see Appendix A) recently developed by Mighell. The data in Table 5 is given in intervals of $\Delta V = 0.1$ mag. Since a sampling of $\Delta V = 0.2$ was used to determine the robust median $V-I$ colors, we see that there are actually *two* realizations of the Ursa Minor fiducial sequence given in Table 5 since only *every other row* in that table represents an *independent measurement* of the true Ursa Minor fiducial sequence. The first fiducial sequence is given at $V_{\rm UMi} = 21.6, 21.8, \ldots, 24.8$ mag in Table 5 and is shown with *open diamonds* in Figure 9. The second fiducial sequence is given at $V_{\rm UMi} = 21.7, 21.9, \ldots, 24.9$ mag in Table 5 and is shown with *open squares* in Figure 9.

We compare the Ursa Minor fiducial sequences (Table 5) with those of the ancient metal-poor Galactic globular cluster M92 (Table A1 in Appendix A) in Figure 9. We get an excellent fit of the Ursa Minor fiducial sequences to the M92 fiducial sequences when we make the M92 fiducial sequence fainter by $\Delta V = 4.60$ mag and add a small color offset of $\Delta(V-I) = 0.01$ mag. We show below that the fit is so good that these fiducials are statistically equivalent over a 3 magnitude range ($22.0 \leq V_{\rm UMi} < 25.0$ mag) from the base of the red giant branch of Ursa Minor to ~1.7 magnitudes below its main-sequence turnoff. This suggests that the ancient metal-poor Galactic globular cluster M92 is an excellent stellar population analog for the median stellar population of the Ursa Minor dwarf spheroidal galaxy. It would not be surprising if the M92 analogy weakens sometime in the future when deeper observations with smaller photometric scatter are analyzed — especially if these future observations survey a significantly larger fraction of the Ursa Minor galaxy.

3.3. $\Delta V_{\rm UMi-M92}$ and $\Delta(V-I)_{\rm UMi-M92}$

The V magnitude offset, $\Delta V_{\rm UMi-M92}$, and the color offset, $\Delta(V-I)_{\rm UMi-M92}$, between the Ursa Minor dwarf spheroidal galaxy and the Galactic globular cluster M92 may be determined by comparing our fiducial sequences of Ursa Minor (Table 5) and M92 (Table A1). The parameter space may be investigated through the application of the following chi-square statistics:

$$\chi^2_{22.2} \equiv \sum_{j=1}^{14} \frac{\left[\underset{\rm UMi}{(V-I)\,(V_j)} - \underset{\rm M92}{(V-I)'\,(V_j - \Delta V_{\rm UMi-M92})} - \Delta(V-I)_{\rm UMi-M92} \right]^2}{\left[\underset{\rm UMi}{\sigma\,(V_j)} \right]^2 + \left[\underset{\rm M92}{\sigma'\,(V_j - \Delta V_{\rm UMi-M92})} \right]^2} \tag{1}$$

where $V_j \equiv 22.0 + 0.2j$ mag and

$$\chi^2_{22.1} \equiv \sum_{k=1}^{15} \frac{\left[\underset{\rm UMi}{(V-I)\,(V_k)} - \underset{\rm M92}{(V-I)'\,(V_k - \Delta V_{\rm UMi-M92})} - \Delta(V-I)_{\rm UMi-M92} \right]^2}{\left[\underset{\rm UMi}{\sigma\,(V_k)} \right]^2 + \left[\underset{\rm M92}{\sigma'\,(V_k - \Delta V_{\rm UMi-M92})} \right]^2} \tag{2}$$

where $V_k \equiv 21.9 + 0.2k$ mag. The color errors are approximated as

$$\sigma \approx \frac{1.25\,\mathrm{adev}}{\sqrt{n}} \tag{3}$$

where adev is the average deviation (column 3 of Tables 5 and A1) and n is the number of stars in the subsample (column 6 of Tables 5 and A1). We use cubic spline interpolations wherever the M92 fiducial sequence (Table A1) does not have a tabulated value at V magnitude values of $V_j - \Delta V_{\rm UMi-M92}$ mag and $V_k - \Delta V_{\rm UMi-M92}$ mag. Usage of cubic spline interpolations is denoted by prime superscripts over the appropriate terms in the definitions of these chi-square statistics.

We now use these chi-square statistics to determine the V magnitude and $V-I$ color offset between Ursa Minor and M92. Tables 6 and 7 give the reduced chi-square values $\chi^2_{22.2}/14$ and $\chi^2_{22.1}/15$, respectively, using V magnitude offsets of $4.400 \leq \Delta V_{\rm UMi-M92} \leq 4.800$ mag and color offsets of $-0.010 \leq \Delta(V-I)_{\rm UMi-M92} \leq 0.030$ mag. The residuals of individual fits (see footnotes a–i in Tables 6 and 7) are shown in Figure 10.

Tables 6 and 7 indicate that a color offset of $\Delta(V-I)_{\rm UMi-M92} = +0.010$ mag always produces the lowest reduced chi-square value — at any given V magnitude offset. This is clearly seen in Figure 10. The residuals systematically become more negative as the color offset is increased from -0.01 to +0.03 mag; the residual scatter is minimized (the best fits occur) at +0.01 mag. We have thus established that the color offset between Ursa Minor and M92 is approximately +0.01 mag.

The top-center panel of Figure 10 shows that a V magnitude offset of $\Delta V_{\rm UMi-M92} = 4.5$ mag and a $V-I$ color offset of $\Delta(V-I)_{\rm UMi-M92} = +0.010$ mag gives systematically large *positive*

residuals in the range $22 \leq V \lesssim 23$ mag. This poor fit in the subgiant branch region of Ursa Minor indicates that the UMi SGB is systematically *fainter* than the shifted M92 SGB. We have thus established a lower limit of the V magnitude offset between Ursa Minor and M92: $\Delta V_{\rm UMi-M92} \gtrsim 4.5$ mag.

The bottom-center panel of Figure 10 shows that using offsets of $\Delta V_{\rm UMi-M92} = 4.7$ mag and $\Delta(V-I)_{\rm UMi-M92} = +0.010$ mag gives systematically large *negative* residuals in the range $22 \leq V \lesssim 23$ mag. This poor fit in the subgiant branch region of Ursa Minor indicates that the UMi SGB is systematically *brighter* than the shifted M92 SGB. We have thus established an upper limit of the V magnitude offset between Ursa Minor and M92: $\Delta V_{\rm UMi-M92} \lesssim 4.7$ mag.

The 90%, 95%, and 99% confidence limits ($\chi^2_{22.2}/14$: 1.50, 1.69, and 2.08) of the fits given in Table 6 are shown in Figure 11. Table 6 shows that fits assuming a V magnitude offset of $\Delta V_{\rm UMi-M92} = 4.575$ mag produce the smallest reduced chi-square value for any given $V-I$ color offset. This is clearly seen in Figure 11 where the confidence contours are widest at the same V magnitude offset.

The 90%, 95%, and 99% confidence limits ($\chi^2_{22.1}/15$: 1.48, 1.66, and 2.04) of the fits given in Table 7 are shown in Figure 12. Table 7 shows that fits assuming a V magnitude offset of $\Delta V_{\rm UMi-M92} = 4.625$ mag produce the smallest reduced chi-square value for any given $V-I$ color offset. This is clearly seen in Figure 12 where the confidence contours are widest at the same V magnitude offset.

A conservative analysis of Figure 12 yields a determination that the V magnitude offset for the Ursa Minor dSph galaxy from the Galactic globular cluster M92 is $\Delta V_{\rm UMi-M92} = 4.60 \pm 0.03$ mag with 99% confidence limits of $4.500 \leq \Delta V_{\rm UMi-M92} \leq 4.700$ mag. Similarly, a conservative estimate of the $V-I$ color offset between Ursa Minor and M92 is $\Delta(V-I)_{\rm UMi-M92} = 0.010 \pm 0.005$ mag with 99% confidence limits of $-0.005 \leq \Delta V_{\rm UMi-M92} \leq 0.020$ mag.

Figure 13 shows our Ursa Minor color-magnitude diagram with the addition of the M92 fiducial sequence of Johnson & Bolte (1998) which has been plotted with a V magnitude offset of 4.6 mag and a $V-I$ color offset of 0.01 mag. We see that the 4 bright blue stars near $V \approx 20$ mag with colors $(V-I) < 0.3$ mag lie underneath the shifted M92 blue horizontal branch; these stars are probable Ursa Minor horizontal branch stars. The brighter part of the Ursa Minor red giant branch ($V < 22$ mag – where our fiducials were not compared) is seen to be slightly redder than the M92 red giant branch. This could be evidence that Ursa Minor is slightly more metal-rich than M92 — however we caution the reader not to over-interpret such a small sample of Ursa Minor red giants. The current observations can not rule out that the main stellar population of Ursa Minor has the same metallicity as M92.

3.4. Distance, Reddening, and Age of UMi

With an accurate estimate of $\Delta V_{\rm UMi-M92}$ in hand, we are now able to determine the apparent V distance modulus of the Ursa Minor dSph galaxy if we know the apparent V distance modulus of M92: $(m-M)_V^{\rm UMi} \equiv (m-M)_V^{\rm M92} + \Delta V_{\rm UMi-M92}$. The above analysis suggests that the uncertainty in the the V magnitude offset between Ursa Minor and M92 is small ($\sim$0.03 mag). This implies that the largest source of uncertainty in the value of $(m-M)_V^{\rm UMi}$ will probably be the error associated with apparent V distance modulus of M92 itself. Pont et al. (1998) recently estimated $(m-M)_V^{\rm M92} = 14.67 \pm 0.08$ mag from their analysis of *Hipparcos* subdwarf parallaxes. A conservative estimate of the apparent V distance modulus of the Ursa Minor dSph is then $(m-M)_V^{\rm UMi} = (14.67 + 4.60) \pm (0.08 + 0.03) = 19.27 \pm 0.11$ mag.

Let us now assume that the $V-I$ color offset between M92 and Ursa Minor is completely due to reddening. The difference in $B-V$ reddening between M92 and Ursa Minor would then be $\Delta E(B-V)_{\rm UMi-M92} = \Delta(V-I)_{\rm UMi-M92}/1.3 = 0.008 \pm 0.004$ mag assuming that $E(V-I) \approx 1.3\,E(B-V)$ (Dean, Warren, & Cousins 1978). Adopting a $B-V$ reddening for M92, $E(B-V)_{\rm M92} = 0.02 \pm 0.01$ mag (e.g., Stetson & Harris 1988, Bolte & Hogan 1995), we now determine the $B-V$ reddening for Ursa Minor to be $E(B-V)_{\rm UMi} = E(B-V)_{\rm M92} + \Delta E(B-V)_{\rm UMi-M92} = 0.03 \pm 0.01$ mag. The absorption in V is determined to be $A_V^{\rm UMi} = 0.09 \pm 0.03$ assuming that $A_V = 3.1\,E(B-V)$ (Savage & Mathis 1979). Our new $B-V$ reddening estimate for UMi agrees well with previous estimates in the literature: 0.03 mag (Zinn 1981) and $0.02^{+0.03}_{-0.02}$ mag (Nemec, Wehlau, & de Oliveira 1988).

Reddening estimates based on *COBE/DIRBE* and *IRAS/ISSA* data give $E(B-V)$ values of 0.023±0.003 mag and 0.033±0.004 mag at the respective positions of the Ursa Minor[9] dwarf spheroidal galaxy and the Galactic globular cluster M92[10] (Schlegel et al. 1998). The difference between these two values, $\Delta{\rm E}(B-V)_{\rm UMi-M92} = 0.010 \pm 0.005$ mag, agrees well with our own estimate of the difference in $B-V$ reddening (0.008 ± 0.004 mag) which we determined above with a completely different method (fiducial-sequence fitting).

King et al. (1998) recently suggested that the $B-V$ reddening of M92 may be 0.04–0.05 mag greater than canonical values: ${\rm E}(B-V)_{\rm M92} = 0.06$–$0.07$ mag. Reid & Gizis (1998) observed that the standard $B-V$ reddening estimate of M92, $E(B-V)_{\rm M92} = 0.02$ mag, is confirmed by Schlegel et al. (see above paragraph); they also note that high reddening estimate of King et al. is at odds with other studies. Our determination of the $B-V$ reddening difference between UMi and M92 could be consistent with the high reddening estimate of King et al. only if the $B-V$ reddening of UMi is also 0.04–0.05 greater than canonical values. Thus while it is true that reddening is patchy across the sky, it is rather unlikely that both M92 and UMi have *exactly the same amount of extra reddening* beyond that predicted from maps of infrared dust emission. We have thus adopted the

---

[9]Estimate derived at the Galactic longitude and latitude of $(l,b)_{\rm UMi} = (105\overset{\circ}{.}00, 44\overset{\circ}{.}85)$.

[10]Estimate derived at the Galactic longitude and latitude of $(l,b)_{\rm M92} = (68\overset{\circ}{.}34, 34\overset{\circ}{.}86)$.

traditional $B-V$ reddening estimate for M92 for the sake of consistency with Schlegel et al. (1998) and older studies of Galactic extinction (e.g., Burstein & Heiles 1982).

We calculate the distance modulus of the Ursa Minor dwarf spheroidal galaxy to be $(m-M)_0^{\rm UMi} = 19.18 \pm 0.12$ based on $(m-M)_V^{\rm M92} = 14.67 \pm 0.08$ mag (Pont et al. 1998) which was derived assuming $E(B-V)_{\rm M92} = 0.02$ mag and $[{\rm Fe/H}]_{\rm M92} = -2.2$ dex (cf. Caretta & Gratton 1997, Zinn & West 1984). Decreasing the adopted $B-V$ reddening for M92 by 0.01 mag decreases the distance modulus estimate by 0.02 mag and increasing the metallicity for M92 by 0.1 dex increases the distance modulus by 0.03 mag (Pont et al. 1998).

Our new distance estimate for Ursa Minor is in good agreement with previous determinations based on early CCD observations in the 1980's once earlier estimates are placed on the same distance scale. For example, Cudworth, Olszewski, & Schommer (1986) derived a distance modulus for Ursa Minor, $(m-M)_0^{\rm UMi} = 19.0 \pm 0.1$ mag, based on a sliding fit to M92. They also got the same value from their measurement of the V magnitude of the horizontal branch at the RR Lyrae gap, $V_{\rm RR} = 19.7$ mag, their absorption value, $A_V^{\rm UMi} = 0.1$ mag, and the assumption that the absolute V magnitude of the RR Lyraes is $M_V^{\rm RR} = 0.6$ mag. Harris (1996) gives the V magnitude of the horizontal branch of M92 as $V_{\rm HB}^{\rm M92} = 15.10$ mag. With our V magnitude offset value between Ursa Minor and M92, we expect that the V magnitude of the Ursa Minor horizontal is $V_{\rm HB}^{\rm UMi} = 19.70 \pm 0.03$ mag which exactly agrees with the measurement of Cudworth et al. (1986). Our distance modulus estimate for Ursa Minor implies that the absolute visual magnitude of the horizontal branch (at a metallicity of [Fe/H] = −2.2 dex) is $M_V^{\rm HB} = V_{\rm HB}^{\rm UMi} - (m-M)_V^{\rm UMi} = 0.43 \pm 0.12$ mag which is consistent with the Lee, Demarque, & Zinn (1990, hereafter LDZ) distance scale value $M_{V,{\rm LDZ}}^{\rm RR} = 0.17[{\rm Fe/H}] + 0.82 = 0.45$ mag assuming, of course, that $M_V^{\rm HB} \approx M_V^{\rm RR}$. Placing the Ursa Minor distance modulus estimate of Cudworth et al. (1986) on the LDZ distance scale and assuming our V absorption value, $A_V^{\rm UMi} = 0.09 \pm 0.03$, we get a revised estimate of $(m-M)_0^{\rm UMi} = 19.16 \pm 0.11$ mag which is just 0.02 mag lower than our own estimate.

How old is the main stellar population of Ursa Minor? We have shown that the ancient metal-poor Galactic globular cluster M92 is an excellent stellar population analog for the median stellar population of the Ursa Minor dwarf spheroidal galaxy. Continuing further with the M92 analogy, we propose that Ursa Minor and M92 are coeval. The determination of the age of the main population of Ursa Minor reduces then to the problem of determining the age of M92. The Harris et al. (1997) analysis of the Galactic globular clusters NGC 2419 and M92 found that while the full impact of *Hipparcos* data and improving stellar models has yet to be felt, an age range of 12–15 Gyr for the most metal-poor Galactic globular clusters is well supported by the current mix of theory and observations. Last year, Pont et al. (1998) estimated that M92 is 14 Gyr based on their analysis of the luminosities of cluster turnoff and subgiant branch stars. They noted that their age estimate for M92 should probably be reduced by ∼1 Gyr if diffusion is important in the cores of globular cluster stars. Our above analysis used the Pont et al. (1998) distance to M92, and so we now adopt their age estimate for M92. Using the M92 analogy one last time, we

conclude that the age of the main stellar population of the Ursa Minor dwarf spheroidal galaxy is $\sim$14 Gyr old.

4. SUMMARY

The findings of this paper can be summarized as follows:

- Our comparison of the fiducial sequence of the Ursa Minor dwarf spheroidal galaxy with the Galactic globular cluster M92 (NGC 341) indicates that that the median stellar population of the UMi dSph galaxy is metal poor ($[\mathrm{Fe/H}]_{\mathrm{UMi}} \approx [\mathrm{Fe/H}]_{\mathrm{M92}} \approx -2.2$ dex) and ancient ($age_{\mathrm{UMi}} \approx age_{\mathrm{M92}} \approx 14$ Gyr).

- The V magnitude offset and $V-I$ color offset between Ursa Minor and M92 are estimated to be $\Delta V_{\mathrm{UMi-M92}} = 4.60 \pm 0.03$ mag and $\Delta(V-I)_{\mathrm{UMi-M92}} = 0.010 \pm 0.005$ mag.

- The Ursa Minor $B-V$ reddening and the absorption in V are estimated to be $\mathrm{E}(B-V) = 0.03 \pm 0.01$ mag and $A_V^{\mathrm{UMi}} = 0.09 \pm 0.03$ mag assuming that the $B-V$ reddening for M92 is 0.02 ± 0.01 mag.

- We have determined that the distance modulus of the Ursa Minor dwarf spheroidal galaxy is $(m-M)_0^{\mathrm{UMi}} = (m-M)_0^{\mathrm{M92}} + \Delta V_{\mathrm{UMi-M92}} - A_V^{\mathrm{UMi}} = 19.18 \pm 0.12$ mag based on the the adoption of the apparent V distance modulus for M92 of $(m-M)_V^{\mathrm{M92}} = 14.67 \pm 0.08$ mag (Pont et al. 1998). The Ursa Minor dwarf spheroidal galaxy is then at a distance of 69 ± 4 kpc from the Sun.

These *HST* observations indicate that Ursa Minor has had a very simple star formation history consisting mainly of a single major burst of star formation about 14 Gyr ago which probably lasted $\lesssim$2 Gyr. While we may have missed minor younger stellar populations due to the small field-of-view of the WFPC2 instrument, these observations clearly show that most of the stars in the central region Ursa Minor dwarf spheroidal galaxy are ancient. If the ancient Galactic globular clusters, like M92, formed concurrently with the early formation of Milky Way galaxy itself, then the Ursa Minor dwarf spheroidal is probably as old as the Milky Way.

We would like to thank Sylvia Baggett for helping us understand the cause of all the image defects we encountered in these archival images. We thank the anonymous referee whose comments and suggestions have improved this article. We wish to thank Don VandenBerg for bringing to our attention the article on the distance to NGC 6397 by Reid & Gizis which appeared while we were finishing the manuscript. KJM was supported by a grant from the National Aeronautics and Space Administration (NASA), Order No. S-67046-F, which was awarded by the Long-Term Space Astrophysics Program (NRA 95-OSS-16). Figure 1 was created with an image from the Digitized

Sky Survey[11]. This research has made use of NASA's Astrophysics Data System Abstract Service and the NASA/IPAC Extragalactic Database (NED) which is operated by the Jet Propulsion Laboratory at the California Institute of Technology, under contract with NASA.

A. A ROBUST FIDUCIAL-SEQUENCE ALGORITHM

Johnson & Bolte (1998, hereafter JB98) recently published a V versus $V-I$ fiducial sequence for the ancient Galactic globular cluster M92 which is shown in Figure A1 on top of their stellar photometry which was kindly provided to use by Jennifer Johnson. JB98 found that mean and mode fitting proved to be susceptible to outliers due to not having enough stars to form a strong ridge line in some areas of the color-magnitude diagram; their M92 fiducial sequence was determined from the best measured stars and was subsequently drawn by hand and eye. We now demonstrate that, given enough stars, it is possible to obtain similar results with a new robust fiducial-sequence algorithm which we present herein.

The median value of a normal (a.k.a. Gaussian) distribution is the mean value of the distribution. The mean value, ($\bar{x}$), of a *small* nearly-normally-distributed sample is sensitive to the presence of outlier data values; the median value is less sensitive to outliers and is therefore considered to be a more robust statistic than the mean. Likewise, the average deviation (a.k.a. mean deviation), $a \equiv \frac{1}{N}\sum_{i=1}^{N}|x_i - \bar{x}|$, of a nearly-normally-distributed sample is, by definition, less sensitive to outliers than the standard deviation, $\sigma \equiv [\frac{1}{N-1}\sum_{i=1}^{N}(x_i - \bar{x})^2]^{1/2}$, of the sample. The average deviation of a normal distribution is $\sim$0.8 times the standard deviation of the distribution[12] and approximately 98% of a normal distribution is found within 3.0 average deviations of the mean of the distribution[13].

---

[11]Based on photographic data obtained using The UK Schmidt Telescope. The UK Schmidt Telescope was operated by the Royal Observatory Edinburgh, with funding from the UK Science and Engineering Research Council, until 1988 June, and thereafter by the Anglo-Australian Observatory. Original plate material is copyright (c) the Royal Observatory Edinburgh and the Anglo-Australian Observatory. The plates were processed into the present compressed digital form with their permission. The Digitized Sky Survey was produced at the Space Telescope Science Institute under US Government grant NAG W-2166.

[12]The average deviation of a normal distribution with a mean of zero and a standard deviation σ is

$$a = \int_{-\infty}^{\infty} |x| \left[\frac{1}{\sigma\sqrt{2\pi}} e^{-x^2/(2\sigma^2)}\right] dx = \sigma\sqrt{\frac{2}{\pi}}\,.$$

A normal distribution with a standard deviation of one ($\sigma \equiv 1$), in the limit of an infinite number of observations, would thus have an average deviation of $a = \sqrt{2/\pi} \approx 0.7989$.

[13]

$$\int_{-3.0a}^{+3.0a} \left[\frac{1}{\sigma\sqrt{2\pi}} e^{-x^2/(2\sigma^2)}\right] dx \approx \int_{-2.4\sigma}^{+2.4\sigma} \left[\frac{1}{\sigma\sqrt{2\pi}} e^{-x^2/(2\sigma^2)}\right] dx \approx 0.9836\,.$$

A robust estimate of the mean of a nearly-normally-distributed sample can be determined by deriving the median of a subsample of the parent sample that is within 3.0 average deviations of the median of the parent sample. This process can, of course, be repeated until the difference between the parent median and the subsample median is negligibly small. Five iterations will generally suffice for the determination of fiducial sequences from high-quality stellar photometry.

We now apply this algorithm (with 5 iterations) to the M92 $V-I$ color photometry as a function of V magnitude in order to determine its fiducial sequence: $[V_{\rm M}, (V-I)_{\rm M}]$. The algorithm results with 0.2-mag slices in V are given in tabular form in Table A1 and graphically in Figures A2, A3 and A4.

We see that our M92 fiducial sequence (Table A1) matches the fit-by-eye fiducial sequence of JB98 near the main-sequence turnoff region ($18 \leq V \leq 21$) to a remarkable degree with a mean and rms difference of just 0.0004 ± 0.0047 mag. The scatter increases slightly for stars brighter than $V \approx 18$ which is not at all surprising given the small sample sizes present on the subgiant branch and red-giant branch of M92 [see column 6 of Table A1]. At the faintest magnitudes ($V > 21$ mag) on the main-sequence, Figures A3 and A4 indicate that our fiducial sequence M92 is slightly redder than that of JB98. Noting that the numbers of the stars in the sample gradually decreases below $V \approx 21$ even though the M92 stellar luminosity function is known to be increasing over this magnitude range (see, e.g., Stetson & Harris 1988), we see that completeness effects become increasingly significant for the JB98 data below $V \approx 21$ mag. The well-known tendency for faint stars to be measured too bright explains why the algorithm gave redder $V-I$ colors than the fit-by-eye values of Johnson & Bolte who consciously compensated for this effect in their determination of the M92 fiducial sequence (see discussion in §3. of JB98).

REFERENCES

Bahcall, J. N., & Soneira, R. M., 1980, ApJS, 44, 73

Bahcall, J. N., & Soneira, R. M., 1984, ApJS, 55, 67

Bahcall, J. N., Ratnatunga, K. U., Buser, R., Fenkart, R. P., & Spaenhauer, A. 1985, ApJ, 299, 616

Biretta, J., Ritchie, C., & Rudloff, K. 1995, *A Field Guide to WFPC2 Image Anomalies*, WFPC2 Instrument Science Report 95-06 (Baltimore: STScI)

Biretta, J. A. et al. 1996, WFPC2 Instrument Handbook, Version 4.0 (Baltimore: STScI)

Burstein, D., & Heiles, C. 1982, AJ, 87, 1165

Bolte, M., & Hogan, C. J. 1995, Nature, 376, 399

Caretta, E., & Gratton, R. G., 1997, A&AS, 121, 95

Cudworth, K. M., Olszewski, E. W., & Schommer, R. A. 1986, AJ, 92 766

Dean, J. F., Warren, P. R., & Cousins, A. W. J. 1978, MNRAS, 183, 569

Harris, W. E. 1996, AJ, 112, 1487

Harris, W. E., Bell, R. A., VandenBerg, D. A., Bolte, D. A., Stetson, P. B., Hesser, J. E, van den Bergh, S., Bond, H. E., Fahlman, G. g., Richer, H. B. 1997, AJ, 114, 1030.

Holtzman, J. A., Hester, J. J., Casertano, S., Trauger, J. T., Watson, A. J., Ballester, G. E., Burrows, C. J., Clarke, J. T., Crisp, D., Evans, R. W., Gallagher J. S., Griffiths, R. E., Hoessel, J. G., Matthews, L. D., Mould, J. R., Scowen, P. A., Stapelfeldt, K. R., & Westphal, J. A. 1995a, PASP, 107, 156

Holtzman, J. A., et al. Burrows, C. J., Casertano, S., Hester, J. J., Trauger, J. T., Watson, A. M., & Worthey, G. S. 1995b, PASP, 107, 1065

Irwin, J., & Hatzidimitriou, D. 1995, MNRAS, 277, 1354

Johnson, J. A., & Bolte, M. 1998, AJ, 115, 693 (JB98)

Krist, J. 1993, in *Astronomical Data Analysis Software and Systems II*, ASP Conf. Ser., 52, edited by R. J. Hanisch, R. J. V. Brissenden, and J. Barnes (ASP: San Francisco), p. 530

King, J. K, Stephens, A., Boesgaard, A. M., & Deliyannis, C. P. 1998, AJ, 115, 666

Krist, J., & Hook, R. 1997, *Tiny Tim User's Guide Version 4.4* (1997 October)

Kleyna, J. T., Geller, M. J., Kenyon, S. J., Kurtz, M. J., & Thorstensen, J. R., 1998, AJ, 115, 2359

Lee, Y.-W., Demarque, P., & Zinn, R. 1990, ApJ, 350, 155 (LDZ)

Mateo, M. 1998, ARA&A, 36, 435

Mighell, K. J., 1997, AJ, 1997, 114, 1458

Mighell, K. J., & Rich, R. M. 1995, AJ, 110, 1649

Nemec, J. M., Wehlau, A., & de Oiveira, C. M. 1988, AJ, 96, 528

Olszewski, E. W., & Aaronson, M. 1985, AJ, 90, 2221

Pont, F., Mayor, M., Turon, C., and VandenBerg, D. A. 1998, A&A, 329, 87

Ratnatunga, K. U., & Bahcall, J. N. 1985, ApJS, 59, 63

Reid, I. N., & Gizis, J. E. 1998, AJ, 116, 2929

Savage, B. D., & Mathis, J. S. 1979, ARA&A, 17, 73

Schlegel, D. J., Finkbeiner, D. P., & Davis, M. 1998, ApJ, 500, 525

Stetson, P. B. & Harris, W. E. 1988, AJ, 96, 909.
van Agt, S. L. Th. J. 1967, *Bull. Astr. Inst. Netherlands*, 19, 275
Wilson, A. G. 1955, PASP, 67, 27
Zinn, R. 1981, ApJ, 251, 52
Zinn, R., West, M. J., 1984, ApJS, 55, 45

TABLE 1. Observation Log

Field	Data Sets	Filter	Exposure (s)	R.A. (2000.0)	Decl. (2000.0)	V3 (deg)	Observation Date
URSA-MINOR	U2PB0102T	F555W	1000.000	15 08 33.329	+67 12 15.655	309.037	1995 Jul 04 18:28:17
	U2PB0103T		1100.000				1995 Jul 04 18:47:17
	U2PB0105T	F814W	1200.000				1995 Jul 04 19:56:17
	U2PB0106T		1100.000				1995 Jul 04 20:19:17

NOTE. — Units of right ascension are hours, minutes, and seconds, and units of declination are degrees, arcminutes, and arcseconds.

TABLE 2. Average Aperture Corrections $\langle \Delta_r \rangle$ for $r = 2.5$ pixels

Filter	CCD	$\langle \Delta_r \rangle$ (mag)
F555W	WF2	-0.097 ± 0.005
	WF3	-0.122 ± 0.010
	WF4	-0.105 ± 0.005
F814W	WF2	-0.122 ± 0.008
	WF3	-0.153 ± 0.012
	WF4	-0.133 ± 0.008

TABLE 3. Zero-Order ("Breathing") Aperture Corrections δ_r for $r = 2.5$ pixels.

Dataset	Filter	Exposure (s)	δ_r [a] WF2	WF3	WF4
U2PB0102T	F555W	1000.000	−0.018	−0.010	−0.018
U2PB0103T		1100.000	−0.021	−0.012	−0.024
U2PB0105T	F814W	1200.000	−0.022	−0.014	−0.019
U2PB0106T		1100.000	−0.024	−0.020	−0.024

[a]The rms error for all values of δ_r is estimated to be 0.005 mag.

TABLE 4. WFPC2 Stellar Photometry in the Ursa Minor Dwarf Spheroidal Galaxy

ID[a]	V (mag)	σ_V (mag)	$V-I$ (mag)	$\sigma_{(V-I)}$ (mag)	quality flag[b]
206106721	23.897	0.037	0.592	0.057	0
206874812	24.779	0.068	0.830	0.088	1
207053087	24.837	0.074	0.508	0.118	0
207163923	25.161	0.095	0.704	0.137	0
208323316	23.815	0.032	0.584	0.047	2

[a] The left-most digit of the ID gives the WFPC2 chip number (2, 3, or 4) where the star was found. The right-most 4 digits gives the x coordinate of the star multiplied by 10. The remaining 4 digits gives the y coordinate of the star multiplied by 10. For example, the first star has an ID of 206106721 which indicates that it is found on WF2 CCD at the (x, y) location of $(672.1, 61.0)$.

[b]The quality flag is 0 if all four observations were good. A value of 1 indicates that both F555W observations were good but at least one of the F814W observations was probably bad. Similarly, a value of 2 indicates that both F814W observations were good but at least one of the F555W observations was probably bad. A value of 3 indicates that at least one of the F555W observations was probably bad and at least one of the F814W observations was probably bad.

NOTE. Table 4 is published in its entirety in the electronic edition of The Astronomical Journal. A portion is shown here for guidance regarding its form and content.

TABLE 5. Ursa Minor dSph Fiducial Sequence ($\Delta V = 0.2$ mag)

V^{a}_{M} (mag) (1)	$(V-I)^{b}_{M}$ (mag) (2)	adev[c] (mag) (3)	mean[d] (mag) (4)	rms[e] (mag) (5)	n[f] (stars) (6)	V^{g}_{min} (mag) (7)	V^{h}_{max} (mag) (8)
21.6	0.849	0.031	0.864	0.045	5	21.5	21.7
21.7 ...	0.826	0.085	0.807	0.127	4	21.6	21.8
21.8	0.827	0.021	0.823	0.028	5	21.7	21.9
21.9 ...	0.839	0.011	0.835	0.016	6	21.8	22.0
22.0	0.813	0.170	0.698	0.204	6	21.9	22.1
22.1 ...	0.803	0.018	0.798	0.023	4	22.0	22.2
22.2	0.787	0.017	0.782	0.023	7	22.1	22.3
22.3 ...	0.787	0.016	0.773	0.019	6	22.2	22.4
22.4	0.741	0.027	0.739	0.036	7	22.3	22.5
22.5 ...	0.697	0.042	0.704	0.049	11	22.4	22.6
22.6	0.656	0.028	0.668	0.034	15	22.5	22.7
22.7 ...	0.639	0.036	0.636	0.048	20	22.6	22.8
22.8	0.597	0.030	0.600	0.038	19	22.7	22.9
22.9 ...	0.589	0.032	0.584	0.039	26	22.8	23.0
23.0	0.570	0.027	0.574	0.034	27	22.9	23.1
23.1 ...	0.569	0.025	0.566	0.031	19	23.0	23.2
23.2	0.570	0.026	0.569	0.032	21	23.1	23.3
23.3 ...	0.567	0.028	0.570	0.035	28	23.2	23.4
23.4	0.571	0.031	0.571	0.039	34	23.3	23.5
23.5 ...	0.565	0.030	0.566	0.037	39	23.4	23.6
23.6	0.567	0.036	0.568	0.045	36	23.5	23.7
23.7 ...	0.588	0.050	0.592	0.059	41	23.6	23.8
23.8	0.591	0.042	0.595	0.050	48	23.7	23.9
23.9 ...	0.603	0.046	0.609	0.056	52	23.8	24.0
24.0	0.622	0.052	0.616	0.065	60	23.9	24.1
24.1 ...	0.627	0.051	0.622	0.067	56	24.0	24.2
24.2	0.631	0.046	0.630	0.058	47	24.1	24.3
24.3 ...	0.631	0.054	0.632	0.064	46	24.2	24.4
24.4	0.650	0.072	0.651	0.088	51	24.3	24.5
24.5 ...	0.672	0.065	0.670	0.082	55	24.4	24.6
24.6	0.678	0.071	0.679	0.087	55	24.5	24.7
24.7 ...	0.639	0.091	0.677	0.106	48	24.6	24.8
24.8	0.696	0.082	0.697	0.101	58	24.7	24.9
24.9 ...	0.722	0.080	0.731	0.101	68	24.8	25.0

[a]Central V magnitude of the subsample of stars defined below.

[b]Median $V-I$ color of the subsample of stars with V magnitudes -0.1 < $[V - V_M] \leq 0.1$ and colors $|(V-I) - (V-I)_M| < 3$ adev.

[c]Average deviation (adev) of the subsample defined above.

[d]Mean (average) of the subsample defined above.

[e]RMS (standard deviation) of the subsample defined above.

[f]Number of stars in the subsample defined above.

[g]Minimum V magnitude (exclusive) of the subsample defined above.

[h]Maximum V magnitude (inclusive) of the subsample defined above.

TABLE 6.
Reduced chi-square values: $\chi^2_{22.2}/14$

	$\Delta(V-I)_{\rm UMi-M92}$								
$\Delta V_{\rm UMi-M92}$ (mag)	-0.010 (mag)	-0.005 (mag)	0.000 (mag)	0.005 (mag)	0.010 (mag)	0.015 (mag)	0.020 (mag)	0.025 (mag)	0.030 (mag)
4.400	12.62	10.65	9.28	8.54	8.41	8.90	10.01	11.73	14.07
4.425	10.52	8.57	7.23	6.51	6.40	6.90	8.01	9.74	12.08
4.450	8.73	6.83	5.53	4.84	4.76	5.28	6.41	8.16	10.50
4.475	7.28	5.41	4.14	3.48	3.42	3.97	5.12	6.87	9.23
4.500	6.13[a]	4.27	3.02	2.37	2.32[b]	2.88	4.04	5.80	8.16[c]
4.525	5.31	3.44	2.17	1.51	1.46	2.00	3.16	4.92	7.28
4.550	4.87	2.96	1.66	0.98	0.90	1.44	2.59	4.35	6.73
4.575	4.80	2.84	1.51	0.79	0.71	1.24	2.40	4.18	6.58
4.600	4.92[d]	2.95	1.61	0.89	0.81[e]	1.35	2.52	4.32	6.75[f]
4.625	5.12	3.18	1.87	1.19	1.13	1.71	2.90	4.73	7.18
4.650	5.45	3.58	2.33	1.70	1.70	2.32	3.57	5.44	7.94
4.675	5.99	4.19	3.01	2.46	2.53	3.21	4.53	6.46	9.01
4.700	6.72[g]	5.02	3.93	3.46	3.60[h]	4.36	5.74	7.74	10.35[i]
4.725	7.70	6.09	5.09	4.70	4.91	5.74	7.17	9.20	11.85
4.750	9.00	7.48	6.55	6.21	6.48	7.33	8.79	10.83	13.47
4.775	10.56	9.10	8.21	7.91	8.20	9.07	10.52	12.56	15.18
4.800	12.19	10.77	9.92	9.65	9.95	10.83	12.29	14.32	16.92[j]

[a]Residuals are shown in *black* (*blue*) in the top-left panel of Figure 10.
[b]Residuals are shown in *black* (*blue*) in the top-center panel of Figure 10.
[c]Residuals are shown in *black* (*blue*) in the top-right panel of Figure 10.
[d]Residuals are shown in *black* (*blue*) in the middle-left panel of Figure 10.
[e]Residuals are shown in *black* (*blue*) in the middle-center panel of Figure 10.
[f]Residuals are shown in *black* (*blue*) in the middle-right panel of Figure 10.
[g]Residuals are shown in *black* (*blue*) in the bottom-left panel of Figure 10.
[h]Residuals are shown in *black* (*blue*) in the bottom-center panel of Figure 10.
[i]Residuals are shown in *black* (*blue*) in the bottom-right panel of Figure 10.
[j]The 90%, 95%, and 99% confidence limits are 1.50, 1.69, and 2.08, respectively.

TABLE 7.
Reduced chi-square values: $\chi^2_{22.1}/15$

$\Delta V_{\rm UMi-M92}$ (mag)	$\Delta(V-I)_{\rm UMi-M92}$								
	-0.010 (mag)	-0.005 (mag)	0.000 (mag)	0.005 (mag)	0.010 (mag)	0.015 (mag)	0.020 (mag)	0.025 (mag)	0.030 (mag)
4.400	13.80	12.19	11.15	10.66	10.73	11.36	12.55	14.30	16.61
4.425	12.18	10.47	9.33	8.75	8.73	9.27	10.37	12.03	14.26
4.450	10.82	9.01	7.76	7.07	6.95	7.40	8.41	9.98	12.12
4.475	9.61	7.70	6.36	5.59	5.39	5.76	6.69	8.20	10.27
4.500	8.42[a]	6.47	5.09	4.28	4.04[b]	4.37	5.27	6.73	8.77[c]
4.525	7.28	5.35	3.98	3.18	2.95	3.27	4.17	5.63	7.65
4.550	6.40	4.50	3.16	2.38	2.17	2.51	3.42	4.88	6.91
4.575	5.81	3.94	2.62	1.86	1.66	2.02	2.94	4.41	6.45
4.600	5.44[d]	3.58	2.28	1.53	1.34[e]	1.71	2.64	4.12	6.15[f]
4.625	5.28	3.42	2.12	1.38	1.19	1.56	2.48	3.96	6.00
4.650	5.41	3.54	2.23	1.48	1.28	1.65	2.57	4.06	6.10
4.675	5.86	3.97	2.64	1.87	1.67	2.04	2.97	4.47	6.53
4.700	6.48[g]	4.58	3.25	2.49	2.30[h]	2.68	3.63	5.14	7.23[i]
4.725	7.15	5.29	4.00	3.27	3.11	3.52	4.50	6.05	8.16
4.750	7.91	6.11	4.88	4.21	4.11	4.58	5.62	7.22	9.39
4.775	8.83	7.11	5.95	5.36	5.34	5.88	7.00	8.68	10.92
4.800	9.95	8.32	7.25	6.75	6.81	7.44	8.63	10.39	12.72[j]

[a]Residuals are shown in *gray* (*cyan*) in the top-left panel of Figure 10.
[b]Residuals are shown in *gray* (*cyan*) in the top-center panel of Figure 10.
[c]Residuals are shown in *gray* (*cyan*) in the top-right panel of Figure 10.
[d]Residuals are shown in *gray* (*cyan*) in the middle-left panel of Figure 10.
[e]Residuals are shown in *gray* (*cyan*) in the middle-center panel of Figure 10.
[f]Residuals are shown in *gray* (*cyan*) in the middle-right panel of Figure 10.
[g]Residuals are shown in *gray* (*cyan*) in the bottom-left panel of Figure 10.
[h]Residuals are shown in *gray* (*cyan*) in the bottom-center panel of Figure 10.
[i]Residuals are shown in *gray* (*cyan*) in the bottom-right panel of Figure 10.
[j]The 90%, 95%, and 99% confidence limits are 1.48, 1.66, and 2.04, respectively.

TABLE A1. M92 Fiducial Sequence ($\Delta V = 0.2$ mag)

V_M^a (mag) (1)	$(V-I)_M^b$ (mag) (2)	adev[c] (mag) (3)	mean[d] (mag) (4)	rms[e] (mag) (5)	n[f] (stars) (6)	V_{min}^g (mag) (7)	V_{max}^h (mag) (8)
17.0	0.821	0.008	0.819	0.011	6	16.9	17.1
17.1	0.813	0.008	0.816	0.010	9	17.0	17.2
17.2	0.813	0.006	0.812	0.008	6	17.1	17.3
17.3	0.804	0.018	0.804	0.022	9	17.2	17.4
17.4	0.794	0.019	0.797	0.024	7	17.3	17.5
17.5	0.776	0.003	0.775	0.004	7	17.4	17.6
17.6	0.777	0.002	0.776	0.003	6	17.5	17.7
17.7	0.762	0.024	0.752	0.031	6	17.6	17.8
17.8	0.724	0.024	0.723	0.032	10	17.7	17.9
17.9	0.698	0.026	0.688	0.029	16	17.8	18.0
18.0	0.654	0.029	0.654	0.035	22	17.9	18.1
18.1	0.616	0.013	0.611	0.016	24	18.0	18.2
18.2	0.596	0.015	0.596	0.019	26	18.1	18.3
18.3	0.577	0.013	0.576	0.016	37	18.2	18.4
18.4	0.569	0.011	0.569	0.014	45	18.3	18.5
18.5	0.559	0.014	0.559	0.016	36	18.4	18.6
18.6	0.551	0.012	0.553	0.014	56	18.5	18.7
18.7	0.562	0.014	0.560	0.019	82	18.6	18.8
18.8	0.565	0.019	0.565	0.025	86	18.7	18.9
18.9	0.568	0.014	0.567	0.018	65	18.8	19.0
19.0	0.570	0.011	0.571	0.014	59	18.9	19.1
19.1	0.581	0.014	0.579	0.017	76	19.0	19.2
19.2	0.586	0.010	0.587	0.013	73	19.1	19.3
19.3	0.590	0.013	0.592	0.017	72	19.2	19.4
19.4	0.598	0.015	0.599	0.019	79	19.3	19.5
19.5	0.611	0.017	0.610	0.021	101	19.4	19.6
19.6	0.619	0.014	0.618	0.018	102	19.5	19.7
19.7	0.630	0.016	0.629	0.021	109	19.6	19.8
19.8	0.644	0.020	0.646	0.025	121	19.7	19.9
19.9	0.651	0.019	0.652	0.025	128	19.8	20.0
20.0	0.664	0.022	0.665	0.029	143	19.9	20.1
20.1	0.674	0.018	0.675	0.023	132	20.0	20.2
20.2	0.685	0.026	0.687	0.033	138	20.1	20.3
20.3	0.704	0.031	0.705	0.041	141	20.2	20.4
20.4	0.721	0.028	0.720	0.036	141	20.3	20.5
20.5	0.732	0.027	0.733	0.035	147	20.4	20.6
20.6	0.750	0.026	0.749	0.033	155	20.5	20.7
20.7	0.763	0.026	0.764	0.033	185	20.6	20.8
20.8	0.776	0.031	0.777	0.039	172	20.7	20.9
20.9	0.796	0.037	0.800	0.047	174	20.8	21.0
21.0	0.813	0.038	0.816	0.047	203	20.9	21.1
21.1	0.838	0.037	0.837	0.046	205	21.0	21.2
21.2	0.853	0.037	0.857	0.047	202	21.1	21.3
21.3	0.869	0.040	0.874	0.049	200	21.2	21.4
21.4	0.889	0.047	0.891	0.059	190	21.3	21.5
21.5	0.915	0.047	0.912	0.059	170	21.4	21.6
21.6	0.939	0.050	0.938	0.064	182	21.5	21.7
21.7	0.954	0.044	0.955	0.056	167	21.6	21.8
21.8	0.971	0.044	0.974	0.054	165	21.7	21.9
21.9	1.002	0.049	1.007	0.061	171	21.8	22.0
22.0	1.028	0.050	1.030	0.062	153	21.9	22.1
22.1	1.050	0.060	1.047	0.075	166	22.0	22.2
22.2	1.064	0.062	1.067	0.075	171	22.1	22.3
22.3	1.083	0.060	1.085	0.073	155	22.2	22.4
22.4	1.100	0.064	1.099	0.077	134	22.3	22.5
22.5	1.132	0.069	1.130	0.086	126	22.4	22.6

[a]Central V magnitude of the subsample of stars defined below.

[b]Median $V-I$ color of the subsample of stars with V magnitudes $-0.1 < [V - V_M] \leq 0.1$ and colors $|(V-I) - (V-I)_M| < 3\,\mathrm{adev}$.

[c]Average deviation (adev) of the subsample defined above.

[d]Mean (average) of the subsample defined above.

[e]RMS (standard deviation) of the subsample defined above.

[f]Number of stars in the subsample defined above.

[g]Minimum V magnitude (exclusive) of the subsample defined above.

[h]Maximum V magnitude (inclusive) of the subsample defined above.

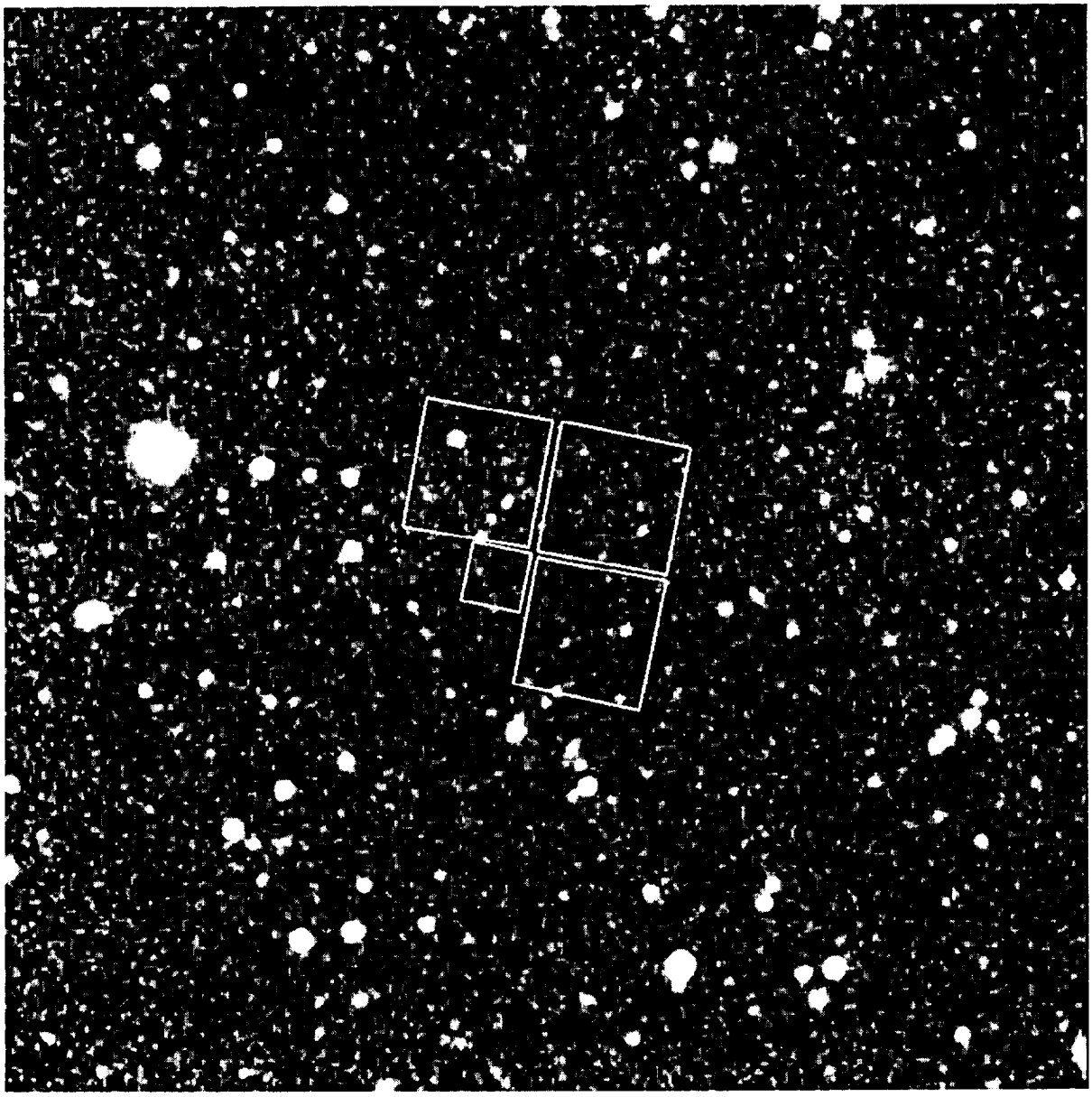

Fig. 1.— Digitized Sky Survey image of the Ursa Minor dwarf spheroidal galaxy with the outlines indicating the *Hubble Space Telescope* WFPC2 observation (see Table 1). The entire field shown subtends 10′ on a side. The orientation is North to the top and East to the left.

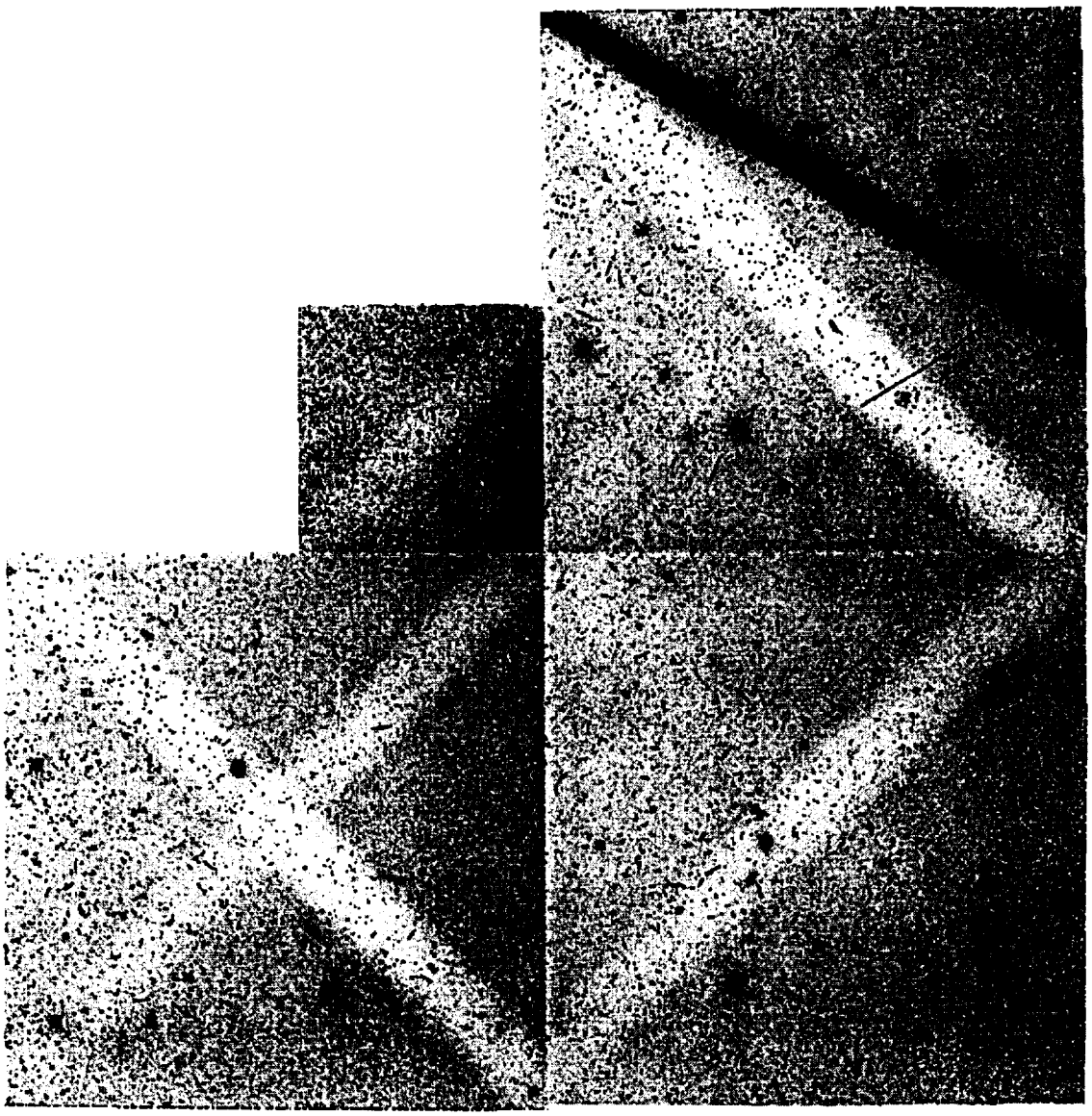

Fig. 2.— A negative mosaic image of the U2PB0103T dataset.

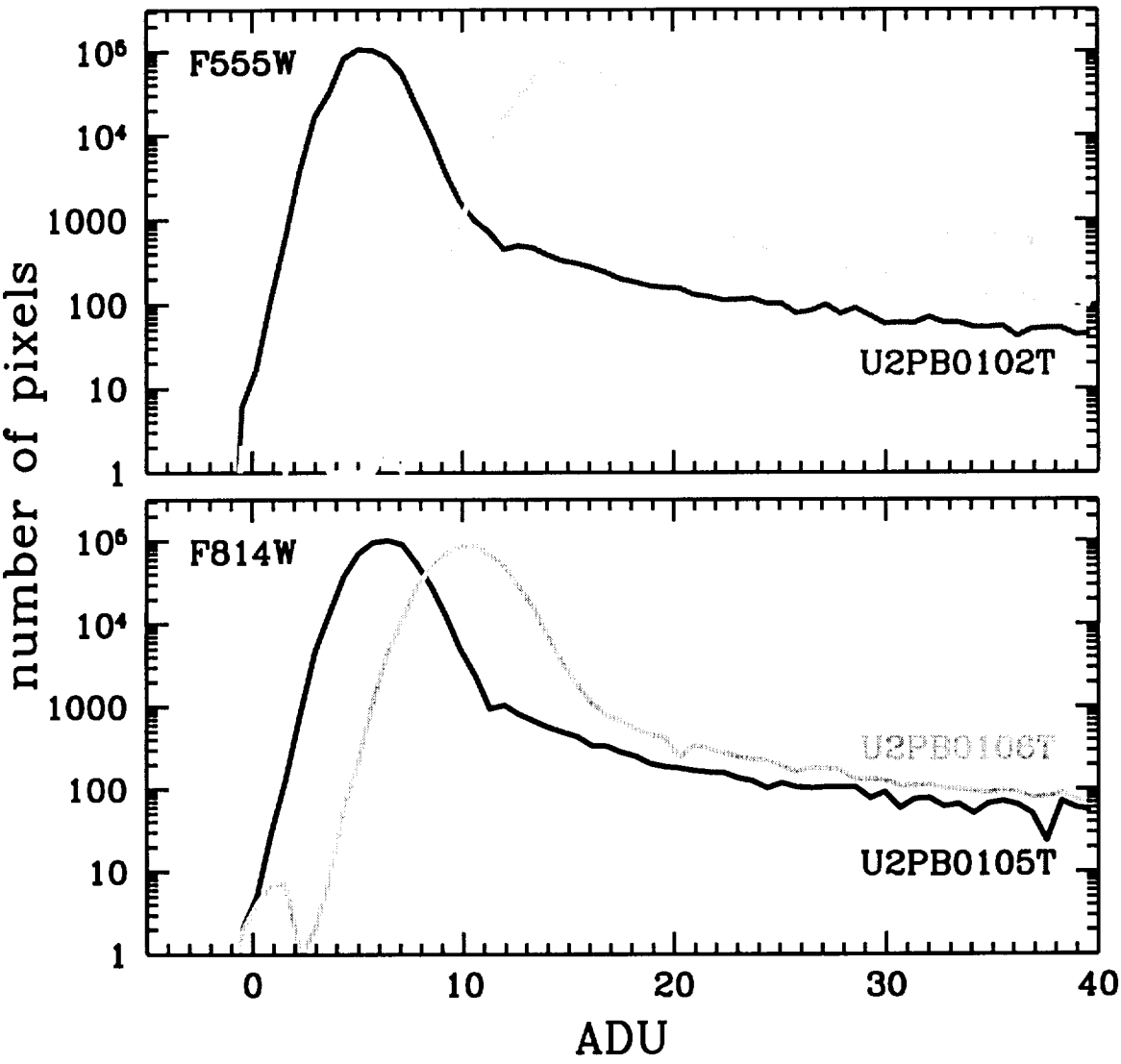

Fig. 3.— The faint portion of the intensity histograms of the WF3 region [60 : 790, 60 : 790] of the datasets given in Table 1. The background "sky" brightened significantly with time.

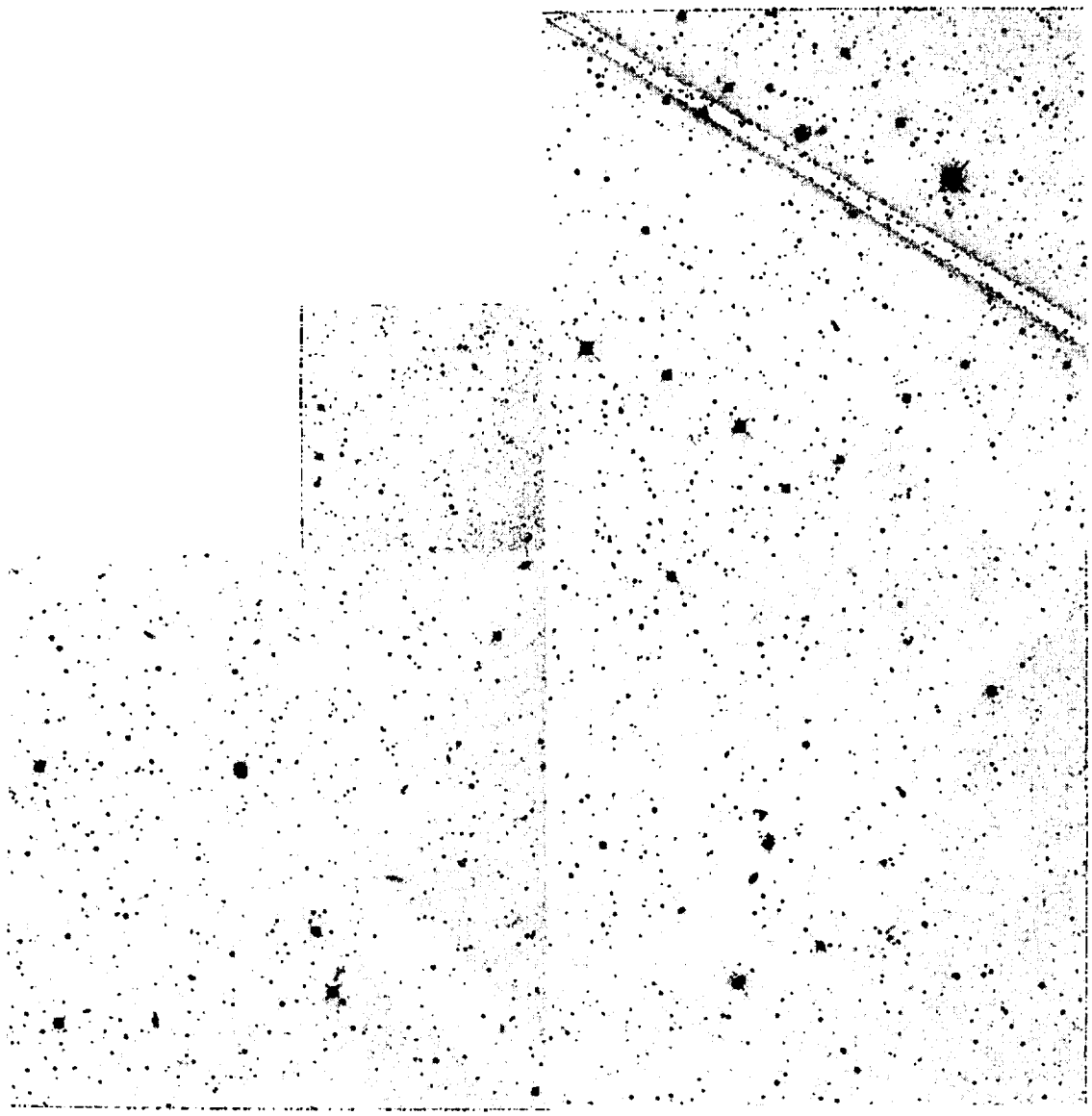

Fig. 4.— The clean combined F555W image created with the STSDAS CRREJ task.

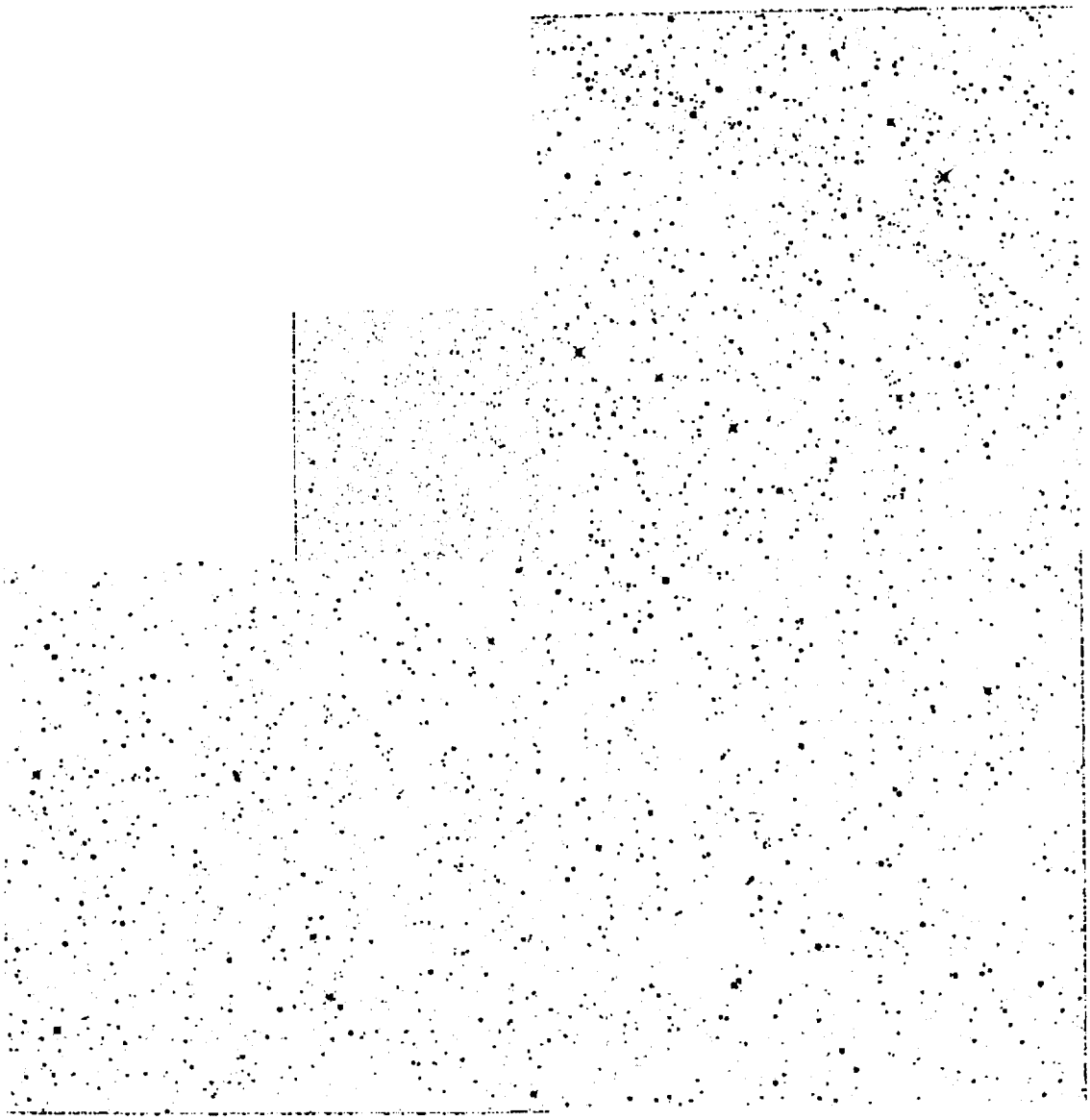

Fig. 5.— The unsharp mask image of Fig. 4. This image was created with the LPD (low-pass difference) digital filter (Mighell & Rich 1995).

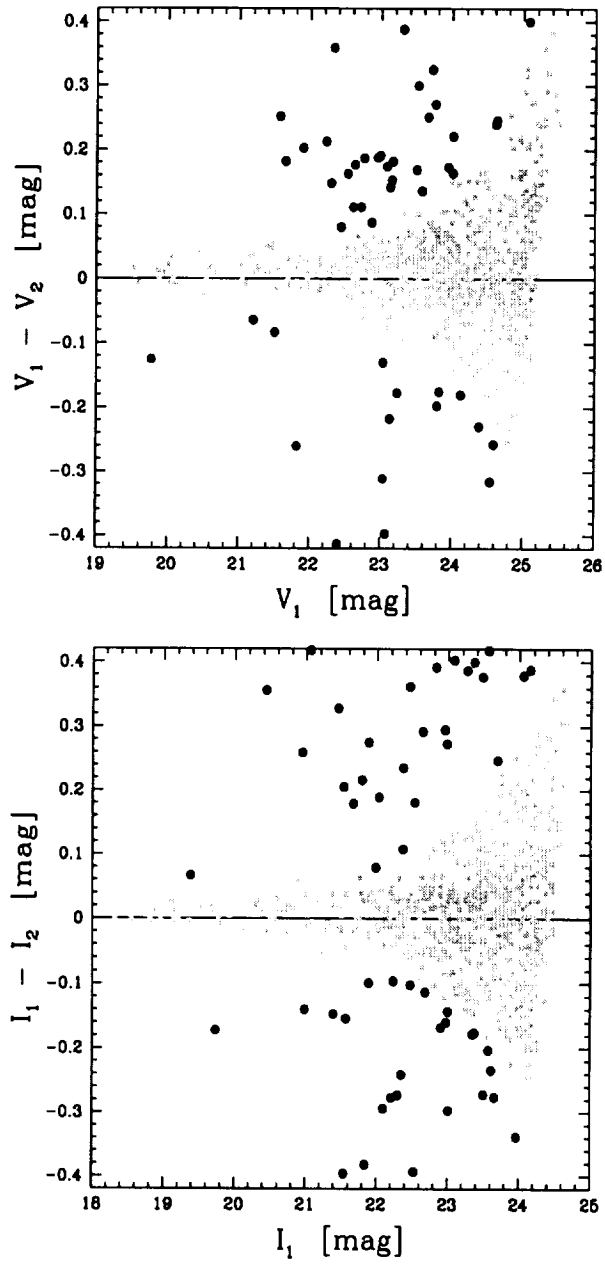

Fig. 6.— Comparison of the VI photometry based on the independent magnitude measurements (V_1, I_1) and (V_2, I_2) which were derived from the respective observations (U2PB0102T,U2PB0105T) and (U2PB0103T,U2PB0106T). The *gray*(*green*) *squares* indicate stars that have good photometry in both observations. The *black*(*blue*) *circles* show probable outlier values which have poor photometry in at least one of the observations.

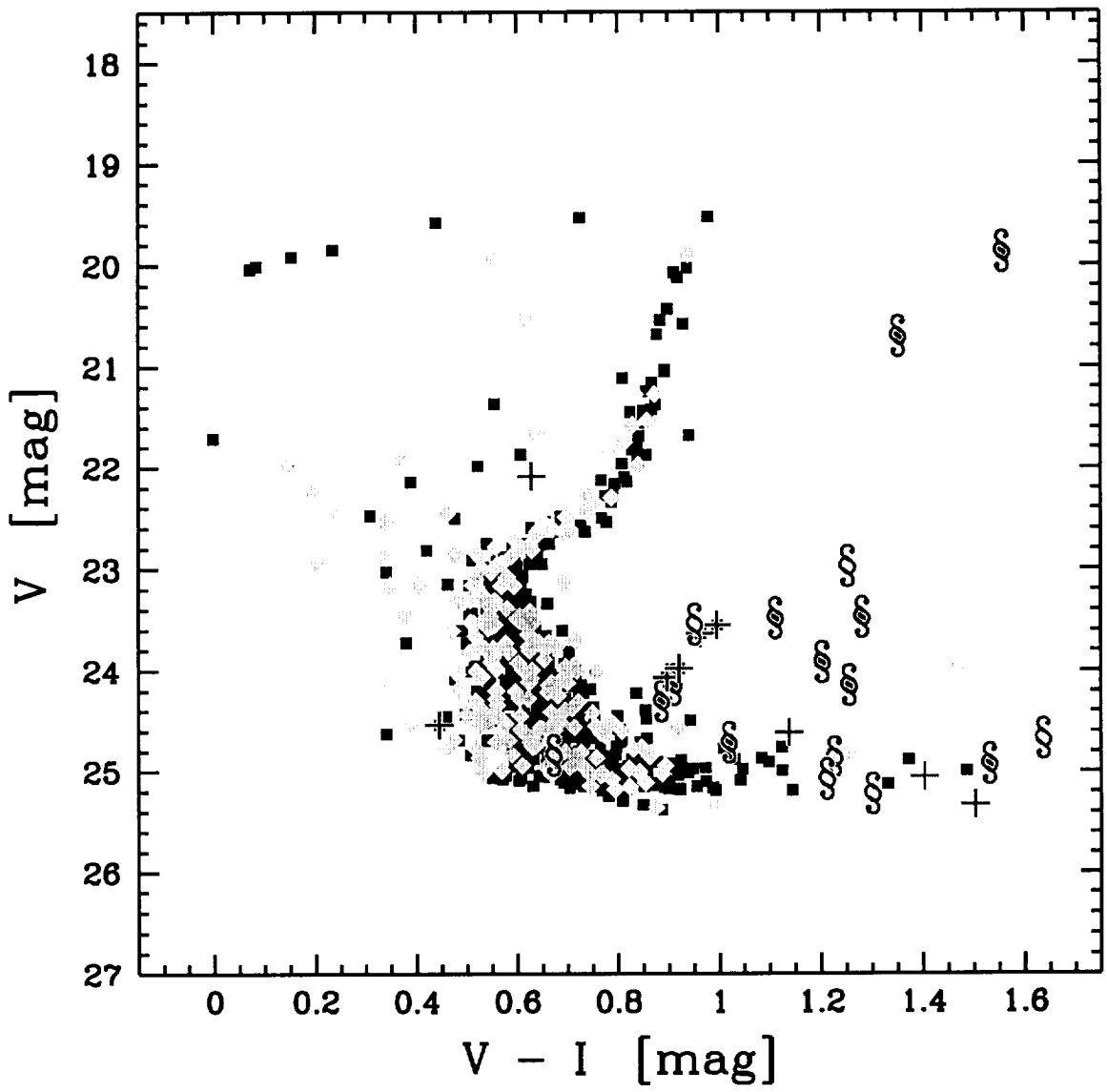

Fig. 7.— The preliminary V versus $V-I$ color-magnitude diagram of the observed stellar field in Ursa Minor dwarf spheroidal galaxy. The 503 *black* (*blue*) *squares* are objects with good photometry in all four observations. The 219 *gray* (*green*) *diamonds* are objects where at least one of the observations was flagged as a probable outlier in Figure 6. The 17 objects overlayed with § symbols are probable galaxies; the 9 + symbols indicate hot pixels.

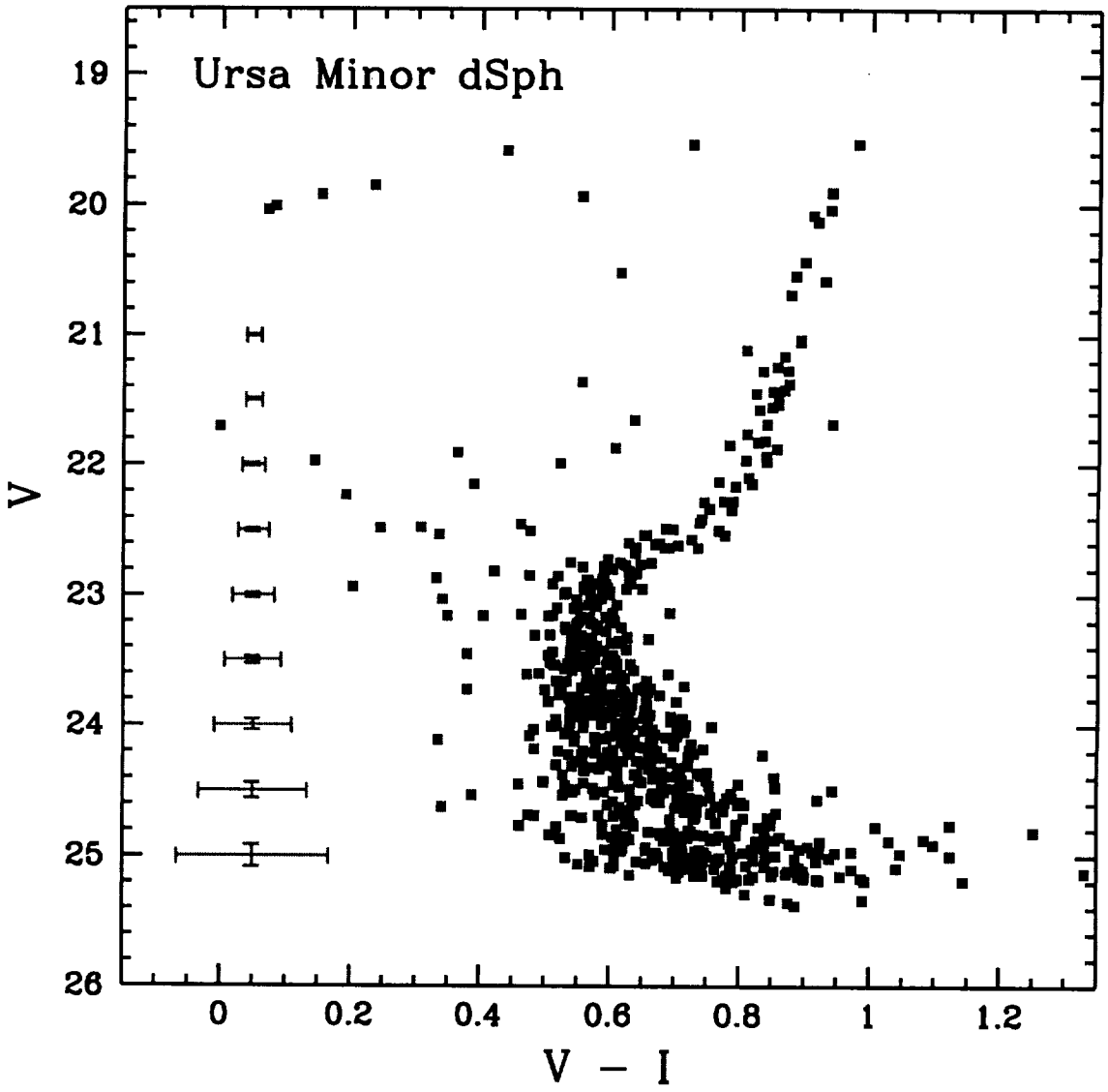

Fig. 8.— The V versus $V-I$ color-magnitude diagram of the Ursa Minor dwarf spheroidal galaxy. The error bars indicate rms ($1\,\sigma$) uncertainties for a single star at the corresponding magnitude.

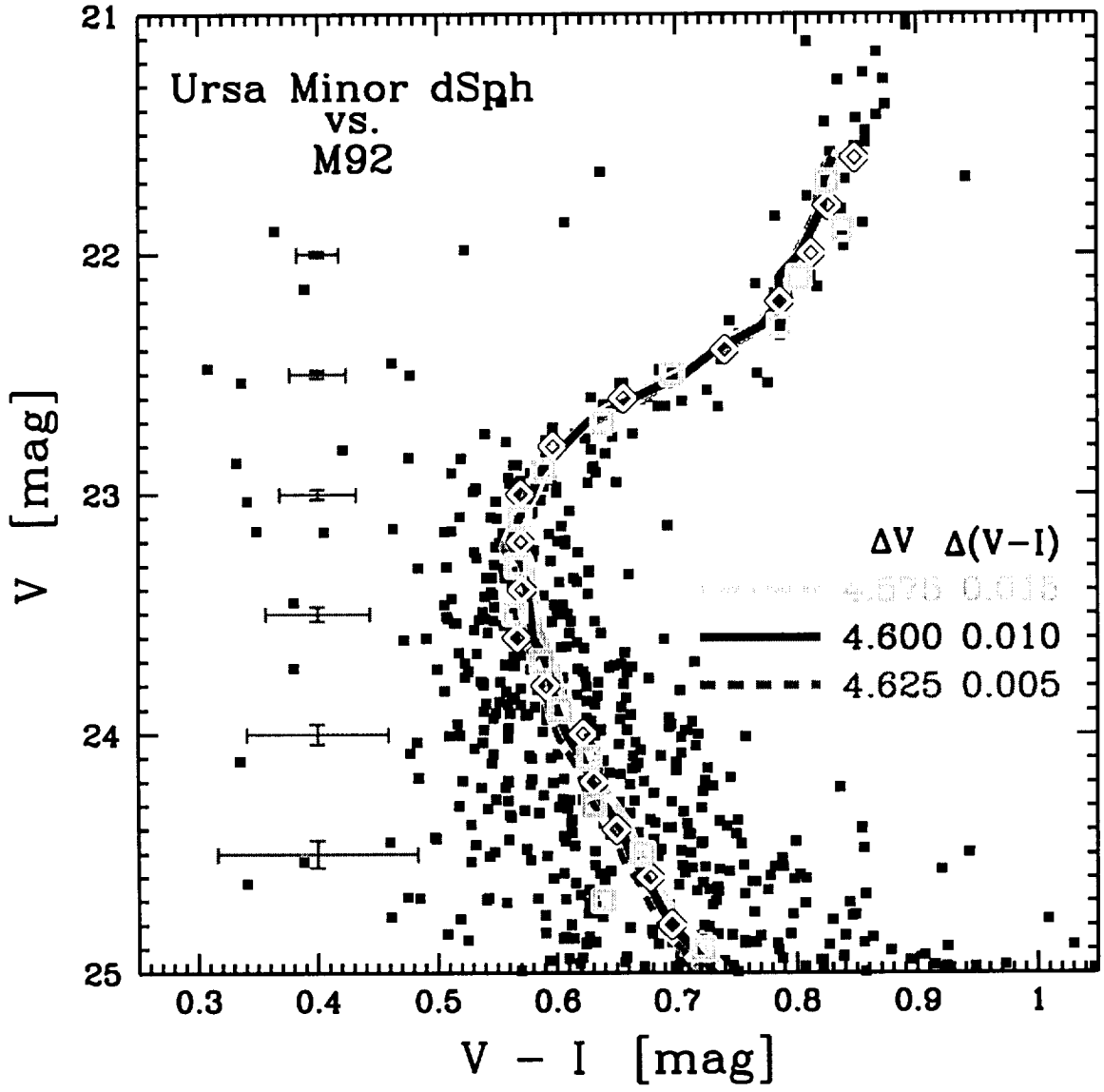

Fig. 9.— An expanded version of Figure 8 with the two Ursa Minor fiducial sequences (Table 5) shown with *open diamonds* ($V_{\rm UMi}$ = 21.6, 21.8, ..., 24.8 mag) and *open squares* ($V_{\rm UMi}$ = 21.7, 21.9, ..., 24.9 mag). We also show, for the sake of comparison, the M92 fiducial sequence (Table A1 of Appendix A) which has been plotted (*curves from left to right*) assuming a shift in $V-I$ color (from M92 to UMi) of 0.005, 0.010, and 0.015 mag and a shift in V magnitude of 4.625, 4.600, 4.575 mag, respectively.

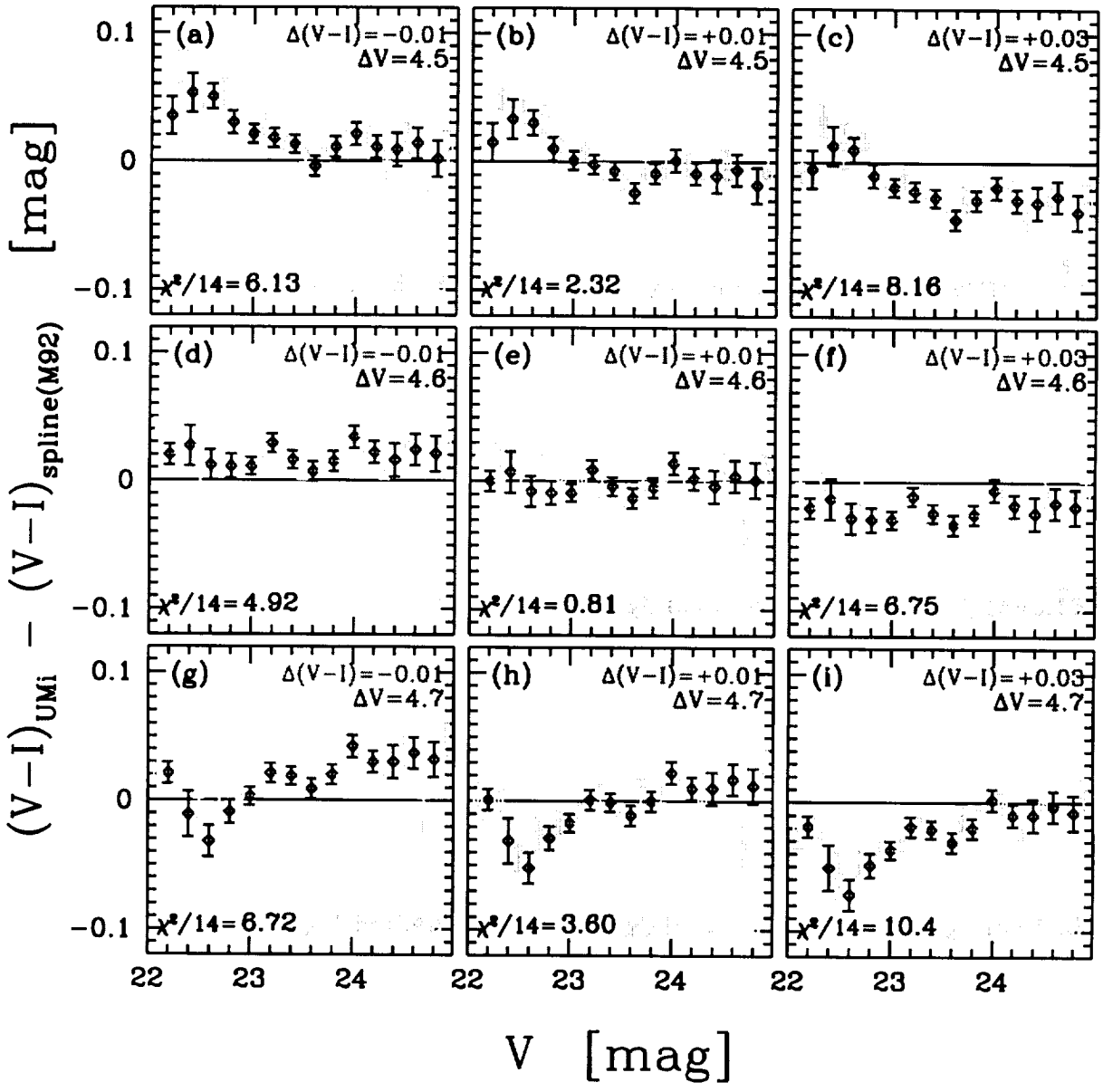

Fig. 10.— The residuals of individual fits from Tables 6 and 7. The residuals of fits marked with footnotes a–i in those tables are shown here in panels (a)–(i). The *black* (*blue*) residuals are from Tables 6 and their reduced chi-square values are shown in the bottom-left corner of each panel. The *gray* (*cyan*) residuals are from Tables 7 and their reduced chi-square values are shown in the bottom-right corner of each panel. The assumed V magnitude offset and $V-I$ color offset between Ursa Minor and M92 is displayed in the top-right corner of each panel.

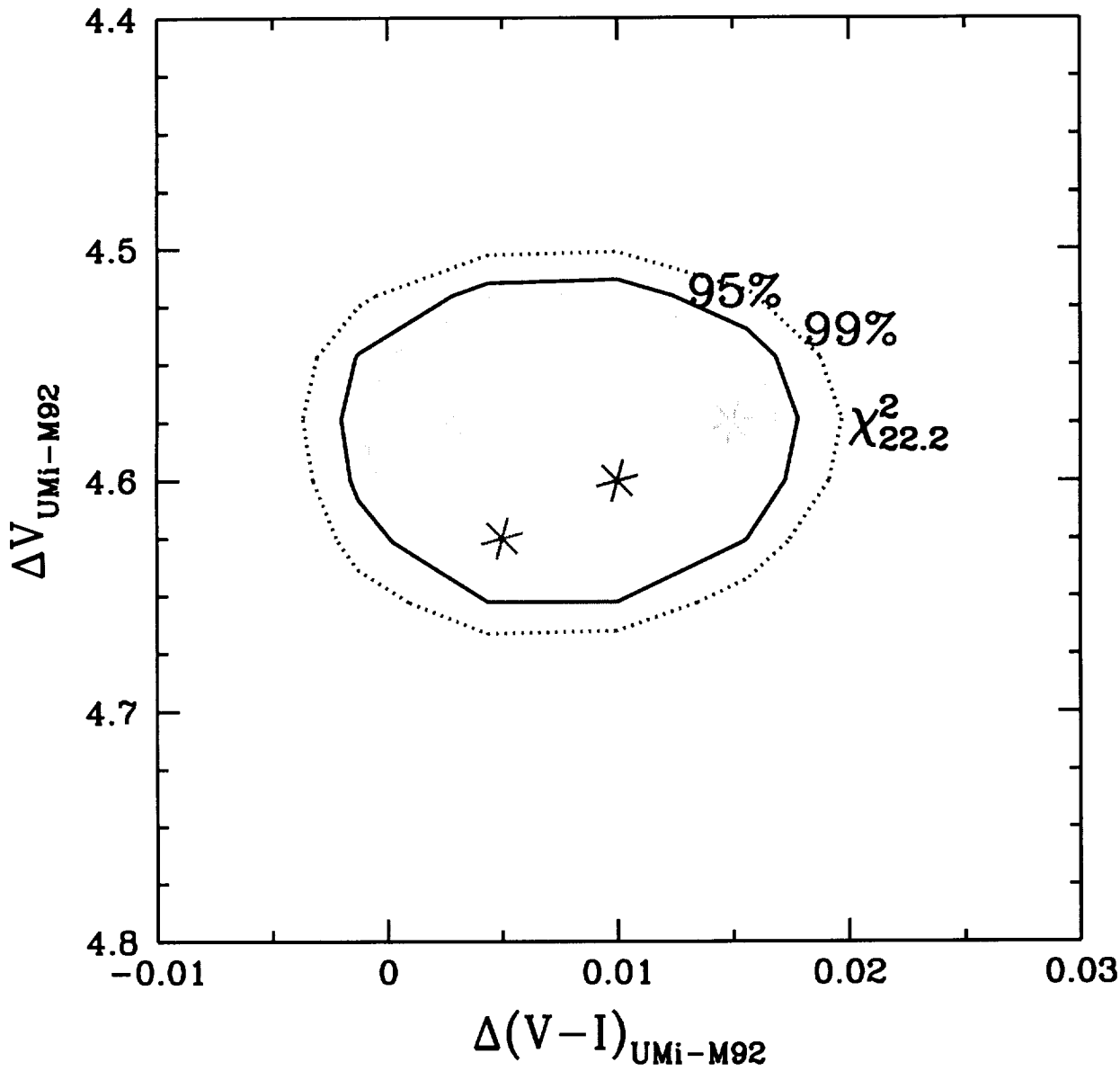

Fig. 11.— The 90%, 95%, and 99% confidence limits of the fits given in Table 6 are shown, respectively, with *dashed, solid, dotted curves.* The fits associated with the three shifted M92 fiducials shown in Figure 9 are displayed here with $*$ symbols. Note that all three fits are found within the 90% confidence limit.

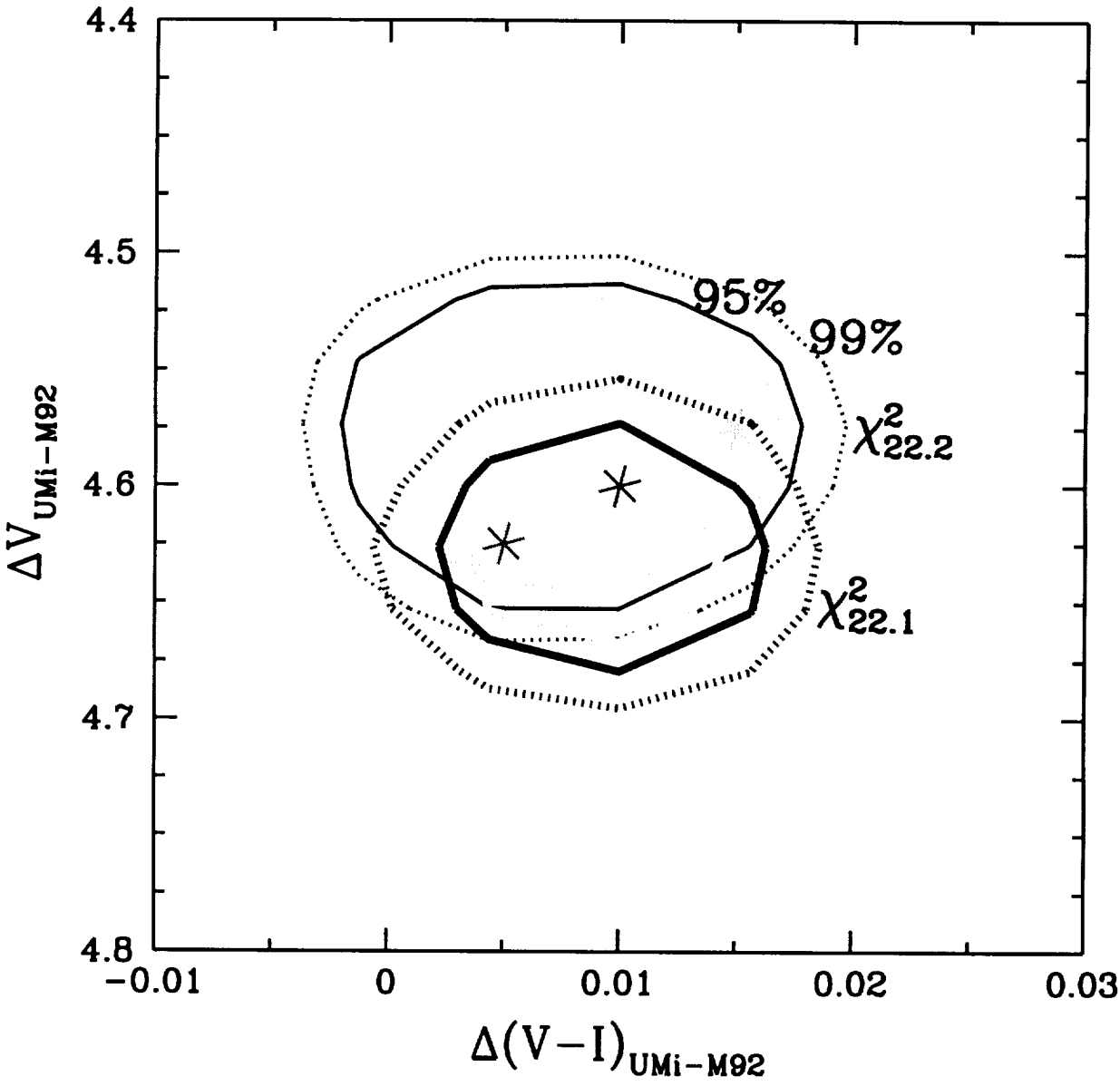

Fig. 12.— Same as Figure 11 with the addition of the 90%, 95%, and 99% confidence limits of the fits given in Table 7 being shown, respectively, with **thick** *dashed, solid, dotted curves.*

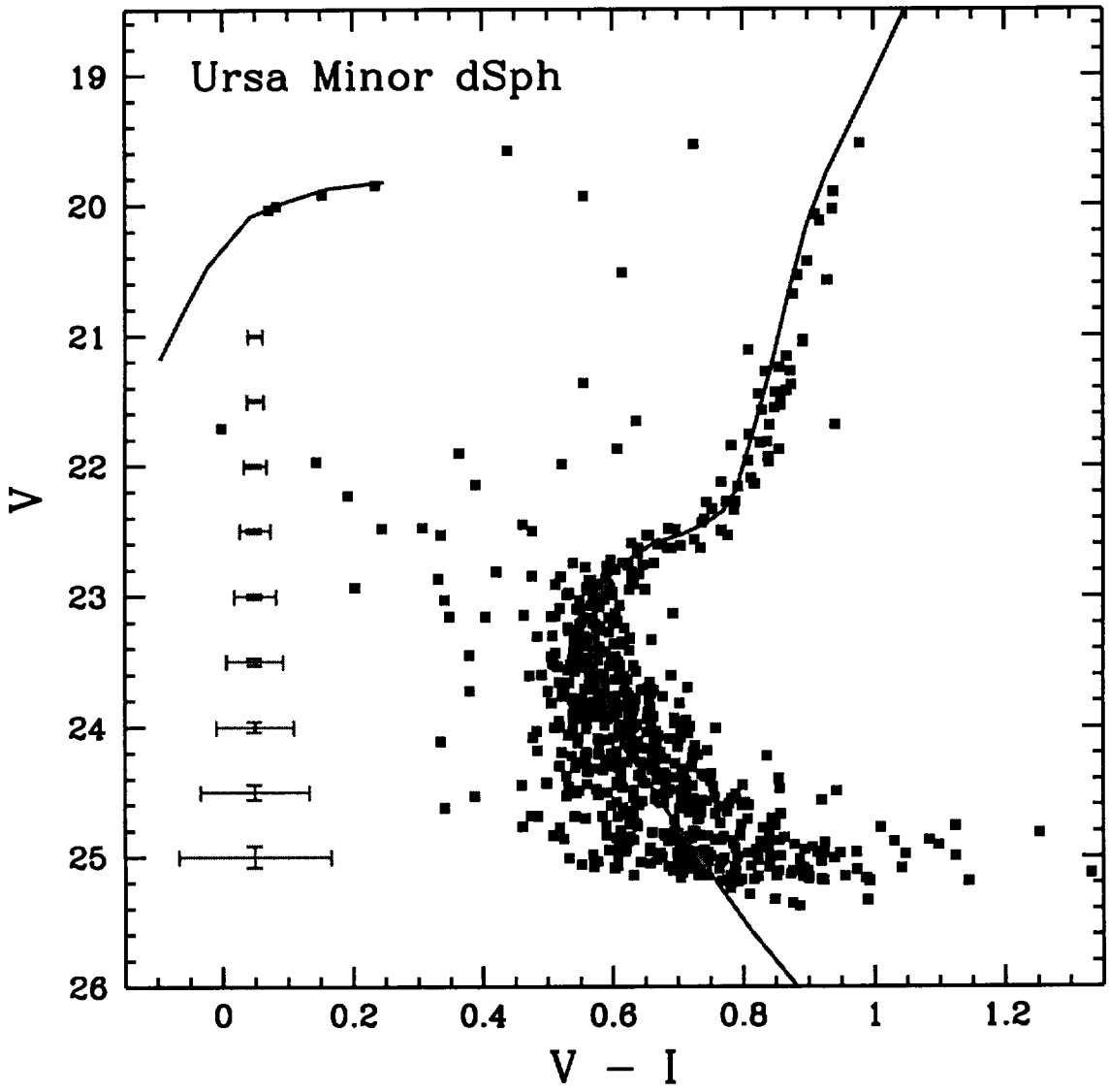

Fig. 13.— Same as Fig. 8 with the addition of the M92 fiducial sequence of Johnson & Bolte (1998) which has been plotted with a V magnitude offset of 4.6 mag and a $V - I$ color offset of 0.01 mag. Only the Ursa Minor stars in the range $22 \leq V \leq 25$ mag and M92 stars fainter than $V = 17.6$ mag (see Fig. A1) were used for the comparison of the fiducial sequences.

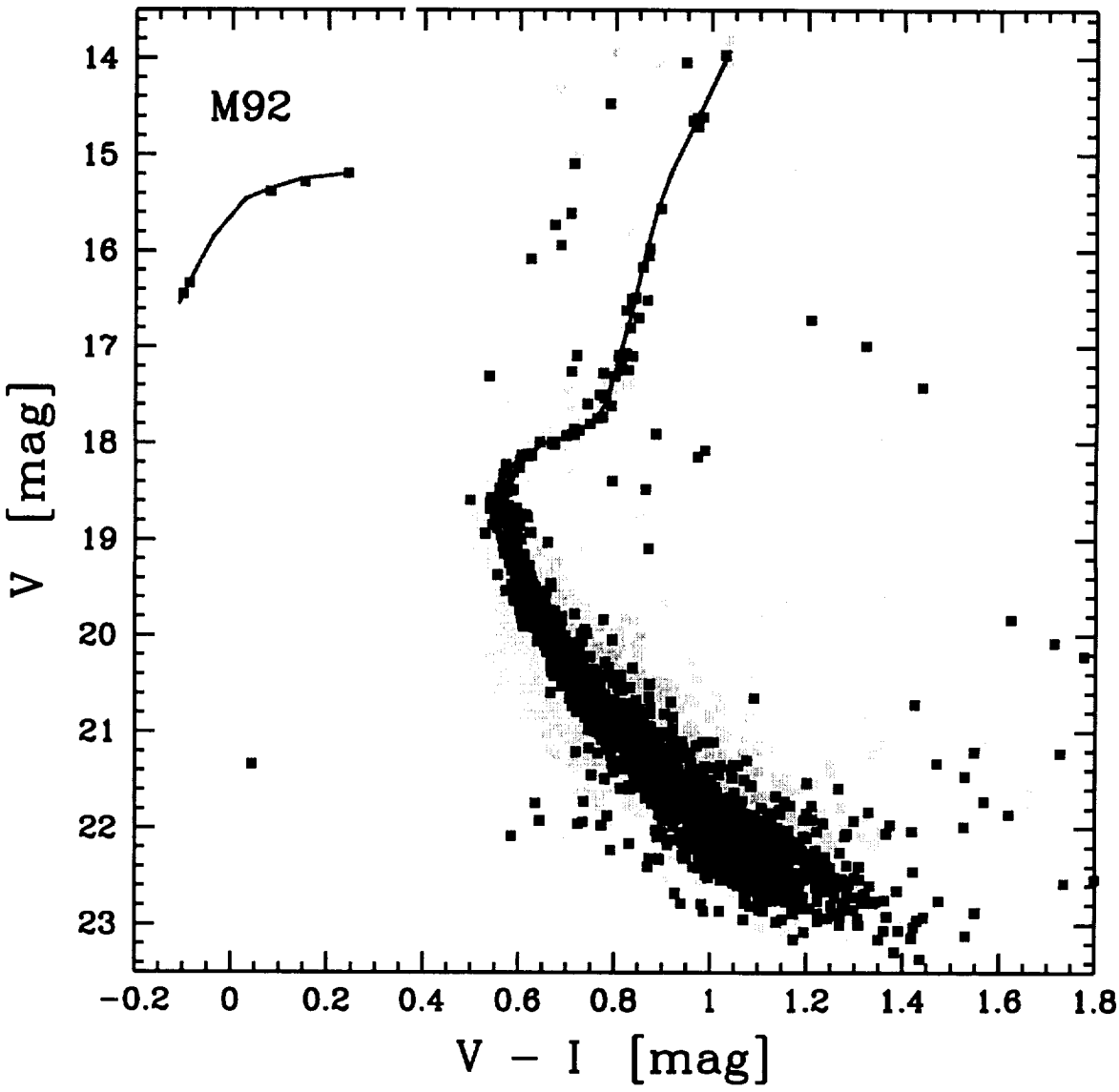

Fig. A1.— The M92 fiducial sequence of Johnson & Bolte (1998; hereafter JB98) is shown as the *gray* (*red*) *curve* on top of their M92 stellar photometry. The *dark gray* (*blue*) *squares* are the stars with the best photometry: 2008 out of 3581 stars had $\geq$14 observations *and* DAOPHOT parameter CHI values $\leq$1.3 . The *gray* (*turquoise*) *squares* are the remaining stars with lower quality photometry.

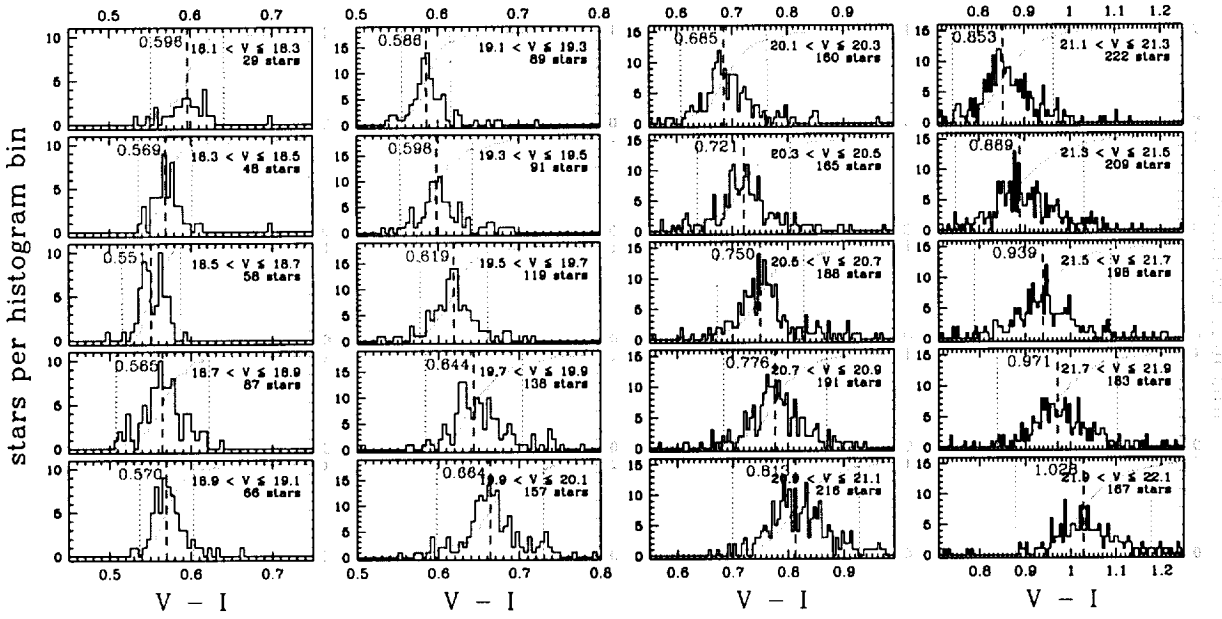

Fig. A2.— Each panel shows a $\Delta V = 0.2$ mag wide subsample of the M92 data of JB98 for $18.1 < V \leq 22.1$ mag in steps of 0.2 mag. The *dark gray* (*blue*) *histogram* in each panel shows the $V - I$ color distribution (in steps of 0.005 mag) of most of the stars within the V magnitude range shown in the upper-right corner of the panel. The total number of stars in each panel is shown in the upper-right corner of the panel below the V magnitude range. The *dashed line* and *4-digit number* in each panel shows the median $V - I$ color, $(V - I)_{\rm M}$ [column 2 of Table A1], of the subsample of stars enclosed within the *dotted lines*. Stars within the dotted lines of each panel all have $V - I$ colors within 3 adev [column 3 of Table A1] of $(V - I)_{\rm M}$. A consistency check is provided in the form of the *gray* (*green*) *cumulative fraction distribution* of the $V - I$ color distribution for all the stars in each panel.

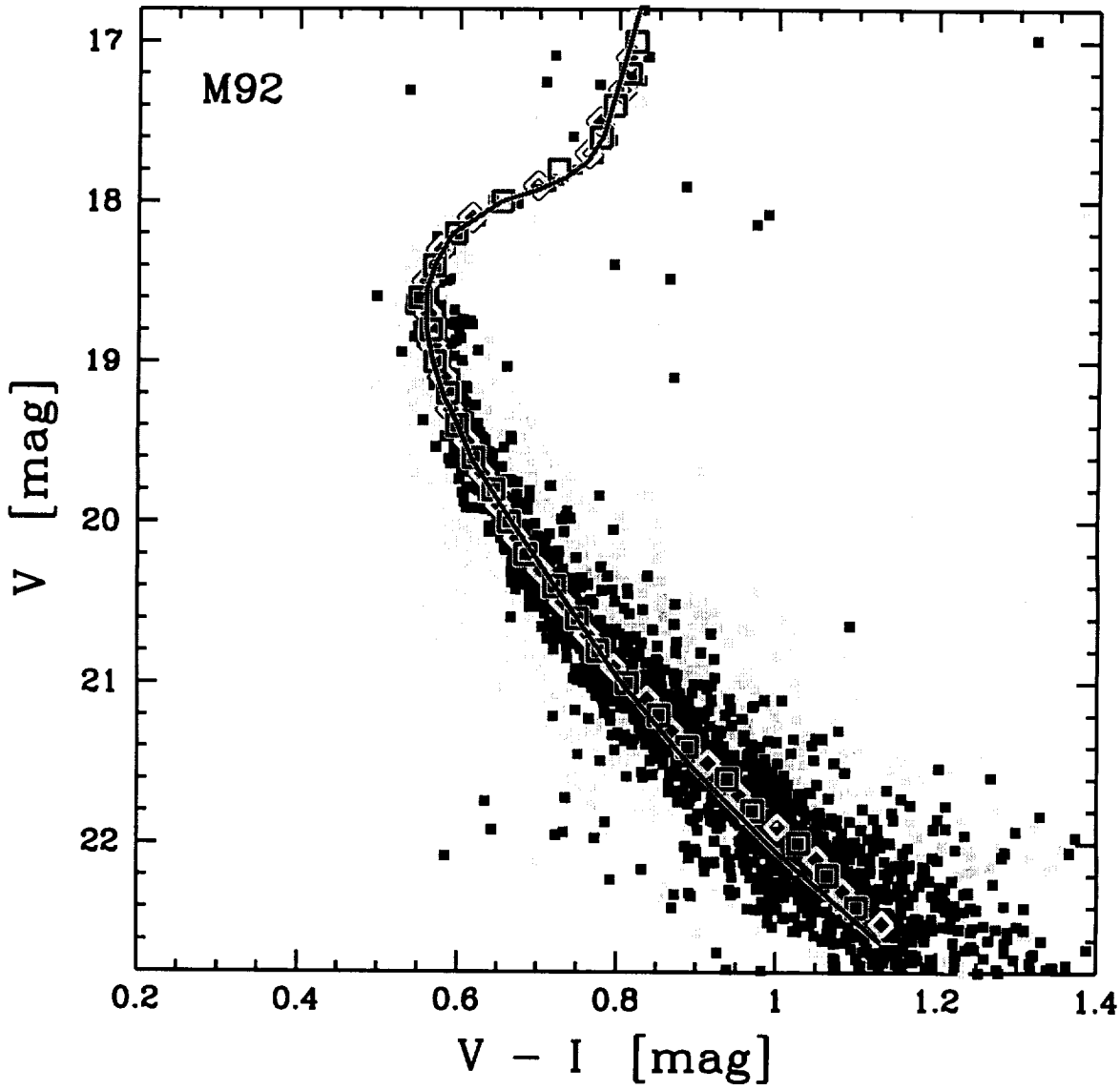

Fig. A3.— The alternating *open squares* and the *open diamonds* plot our M92 fiducial sequence (Table A1). The M92 fiducial sequence of JB98 is shown as the *gray* (*magenta*) *curve*. The best M92 stellar photometry of JB98 (defined in Fig. A1) is shown with *dark gray* (*blue*) *squares* with the remainder shown with *gray* (*turquoise*) *squares*.

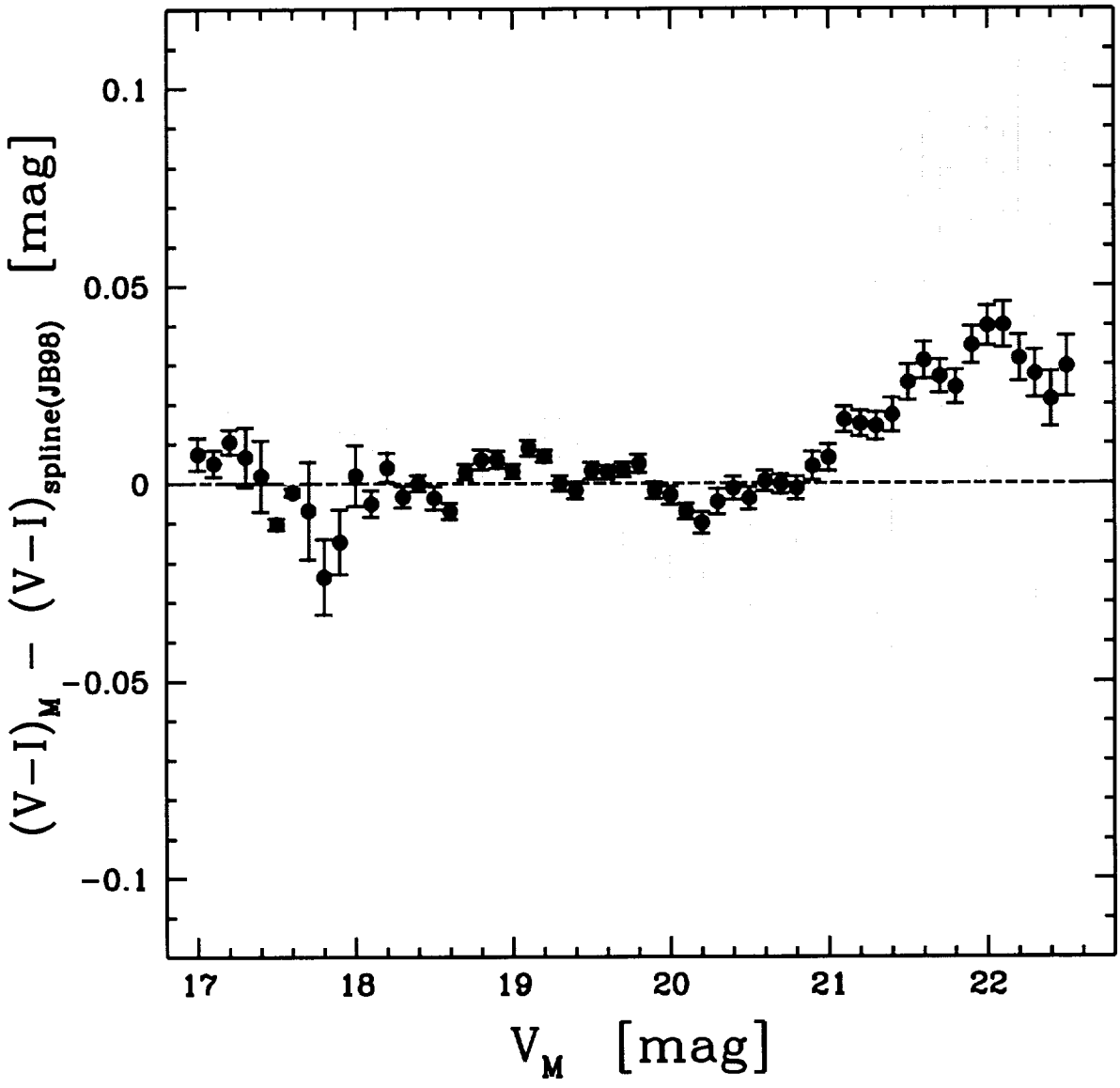

Fig. A4.— The difference between our M92 fiducial sequence Table A1) and a spline fit of the M92 fiducial sequence of JB98. The mean and rms difference over the entire V magnitude range is 0.007 ± 0.014 mag; near the main-sequence turnoff ($18.0 \leq V \leq 21.0$) the mean and rms difference is significantly better: 0.0004 ± 0.0047 mag. The *dark gray* (*blue*) *errorbars* show the lower limit estimate of the 1σ errors [$\sigma \approx (1.25\,\mathrm{adev}/\sqrt{n})$ where adev is the average deviation and n is the number stars in the given subsample (see Table A1). The *light gray* (*cyan*) *errorbars* show the conservative upper limit estimate of the 1σ errors ($\sigma \approx 1.25\,\mathrm{adev}$).